Modelling hydrodynamics in an energetic tidal strait with pronounced bathymetric features

Lucas Mackie[a,*], Paul S. Evans[b], Magnus J. Harrold[c], Tim O'Doherty[d], Matthew D. Piggott[a], Athanasios Angeloudis[e]

[a] *Department of Earth Science & Engineering, Imperial College London, London, UK*
[b] *Intertek Energy & Water, The Maltings, Cardiff, CF24 5EA, UK*
[c] *Offshore Renewable Energy Catapult, Pembroke Dock, UK*
[d] *School of Engineering, Cardiff University, The Parade, Cardiff CF24 3AA, UK*
[e] *School of Engineering, Institute for Infrastructure & the Environment, The University of Edinburgh, Edinburgh, UK*

Abstract

Characterising tidal hydrodynamics in the vicinity of submerged features can be demanding given the hostility of the marine environment. Logistical challenges in the measurement of such flows has promoted research on wake studies through physical and numerical modelling. In this study, site measurements and modelled data are combined to provide an insight into the regional hydrodynamics within a macrotidal strait, namely Ramsey Sound in Pembrokeshire, Wales, UK. The site has received interest from tidal energy developers but is characterised by various steeply inclined bathymetric features, including a semi-submerged pinnacle known as Horse Rock. Understanding how prominent submerged features impact on flow conditions can be crucial for the feasibility and deployment of marine (energy) infrastructure. Observational bed- and vessel-mounted acoustic Doppler current profiler (ADCP) data are used to calibrate a coastal ocean model. The depth-averaged model is generated using *Thetis*, a coastal flow solver based on the finite-element engine *Firedrake*. Hydrodynamic characteristics are examined at different stages of the spring-neap tidal cycle, highlighting the local and regional influence of prominent bathymetric features. In particular, this study focuses on how common assumptions in tidal stream resource assessment models could hinder model calibration. A variable Manning coefficient field is utilised to represent differences in seabed roughness; this is an approach not generally undertaken in similar modelling studies where a uniform constant coefficient is typically calibrated. Also highlighted is the effect of mesh resolution on capturing certain wake structure characteristics, which points to the need to locally refine the mesh around key bathymetric features to a level that is also not typically applied in modelling studies used for tidal resource assessment.

Keywords: Coastal hydrodynamics, field measurements, marine energy, unstructured mesh, wake modelling, Manning coefficient

---

1. Introduction

The eastern coast of the Irish Sea, UK, combines high tidal ranges [1] with an abundance of headlands, islands and reefs, facilitating strong tidal currents suitable for tidal stream energy development [2, 3]. There is an extensive body of research that aims to improve insight into shallow-water flows around water surface-piercing obstacles, through laboratory experiments [4, 5, 6] and field-based observational [7, 8] or modelling [9, 10, 11] case studies around coastal features. Meanwhile, flow in the vicinity of idealised submerged

---

[*] Corresponding author

Email addresses: `l.mackie18@imperial.ac.uk` (Lucas Mackie), `a.angeloudis@ed.ac.uk` (Athanasios Angeloudis) obstacles has been studied experimentally [12], and with numerical modelling [13], highlighting the complexity of unsteady flow and its sensitivity to a series of site-specific parameters, including relative submergence, Reynolds number, obstacle characteristic length scale, aspect ratio, boundary layer roughness characteristics, and free stream turbulence. However, field characteristics of these flows are poorly understood as relatively few field-based studies of the wake characteristics of submerged natural obstacles have been undertaken [14], while even fewer combine these with detailed modelling exercises.

The reduction in streamwise velocity in the lee of an obstacle is termed a wake, with the ensuing effects classified into near- and far- wake regions. Flow reduction is generally at its greatest immediately downstream of the obstruction, with high shear stresses at the wake boundary [15]. The wake widens and flow velocity recovers with distance downstream until the wake effectively disappears, i.e. free-stream velocity downstream of the obstruction recovers to the free-stream velocity upstream (termed “wake recovery”). An idealised wake pattern is seldom observed in regions that are subjected to turbulent and non-uniform flow regimes. Irregular bathymetry and asymmetrical coastlines disturb the wake structure such that quantification of the free-stream velocity downstream of the structure becomes a challenging exercise.

This study focuses on flow conditions around a natural pinnacle within Ramsey Sound, a tidal strait on the Welsh coastline in the UK. A recent governmental report highlights the economic and power potential of developing a marine energy industry in the UK [16]. Ramsey Sound was identified as a prime candidate for harnessing tidal energy. Tidal Energy Ltd previously explored the viability of the strait in terms of its energy output, through the testing of a single 400kW DeltaStream device [17]. The highly dynamic nature of the marine environment has hindered commercial progress, presenting challenges to the timing of maintenance activities and disrupting operation. As a result, further insight into these flow conditions merits research to inform future commercial activities in highly energetic and challenging sites that are focal for the development of the marine energy industry.

Evans et al. [14] discusses how the submerged natural pinnacle, Horse Rock, is of sufficient size for its wake to have an impact on the flow experienced by turbines that could be positioned downstream at certain periods of the tide. As a result, this suggests that under such conditions, tidal stream devices might be within the wake regions exhibiting substantial velocity deficits, impairing the operational performance of the turbines and their expected energy output. Furthermore, such areas can exhibit highly dynamic flow structures [18] potentially contributing to turbine failure [19]. Other potential tidal-energy sites identified in the UK [20], such as the Pentland Firth [21], Rathlin Sound [11] and Kyle Rhea [14], also have physical characteristics similar to those of Ramsey Sound.

Ramsey Sound presents a non-trivial case to simulate and highlight the capabilities and short-comings of typical tidal resource assessment models in representing highly dynamic and localised flow conditions resulting from obstructive bathymetric features. 2D depth-averaged modelling is a computationally efficient [22], and widely used method in marine energy applications for characterising tidal energy resource and investigating suitable deployment locations. In representing the irregular shape of the coastline, such modelling studies often discretise the domain horizontally by an unstructured mesh. These multi-scale numerical models typically refine the mesh to a greater extent in areas of interest, balancing computational cost and/or simplicity with field data configuration precision. For the case study discussed above, and given the short distance over which Horse Rock protrudes horizontally, the minimum mesh element size applied in similar regional, coastal or ocean models [9, 11, 21, 23, 24, 25, 26] would severely misrepresent its shape. The degree of mesh refinement was suitable for their scope and area of focus, but the application of a similar mesh structure on Horse Rock in Ramsey Sound could easily under- and/or over-appreciate the more localised hydrodynamic impact it may have. In these studies, the finest part of the mesh is also generally applied in turbine deployment zones, as opposed to areas containing prominent bathymetric features, furthering the likelihood that an obstruction with similar geometry to Horse Rock would remain under-resolved.

Previous literature examining flow dynamics in and around Ramsey Sound includes Haverson et al. [17] who applied a highly refined mesh around Horse Rock in modelling regional morphological impacts of turbine arrays, and Evans et al. [14], who analysed a comprehensive acoustic Doppler current profiler (ADCP) survey dataset to investigate turbine considerations stemming from flow conditions around Horse Rock. Both recommend 3D modelling to characterise the local hydrodynamics. However, the favourable computational efficiency when depth-averaging offers numerous additional research possibilities, such as advanced array optimisation [27]. In addition, the availability of both vessel- and seabed-mounted ADCP survey data to calibrate the model presents the opportunity to validate over a wide spatial and temporal scale. Common assumptions with regards to certain physical parameters represented in 2D tidal models may inhibit the ability to sufficiently calibrate the model against this available field data. For example, while application of a seabed friction coefficient has previously acknowledged variability [28, 29], it is often applied as either a constant throughout the whole domain [11, 25], or varied solely through additional momentum sinks resembling friction parameterisations as a representation for turbines [17, 21, 24, 26]. The effectiveness of calibrating a depth-averaged model against comprehensive survey data to represent wake hydrodynamics around a prominent but small-scale submerged bathymetric obstruction, through applying both Manning coefficient variability and high localised mesh refinement, warrants analysis.

2. Case study location: Ramsey Sound, Wales, UK

Ramsey Sound is a tidal strait approximately 3km long, ranging in width from 500-1600m. It is connected to the Irish Sea and separates Ramsey Island from the headland of St. David's, Pembrokeshire, Wales (Fig. 1). Key physical characteristics of the tidal strait have previously been noted by Evans et al. [14] and others, and can be observed in Fig. 2c. The water depth generally varies between 20-40m below Lowest Astronomical Tide (LAT) - also commonly referred to as Chart Datum (CD) - but reaches a maximum depth of 66m LAT within a north-south trending trench. A roughly conical submerged pinnacle called Horse Rock dominates the northern portion of the strait (Fig. 3). It rises 23m above the surrounding seabed and has diameters of ∼100m at base and ∼50m at half height (denoted by D). According to Admiralty Charts, it pierces the water at +0.9m LAT [31]. Finally, a shallow rocky reef named "The Bitches" contributes to the narrowing of the straight towards the southern section [14].

Tidal hydrodynamics in the wider Irish sea stem from the superposition of two Kelvin-type waves, resulting in zones exhibiting negligible tidal range but strong tidal currents [2]. Within Ramsey Sound, tidal elevations are a result of a progressive tidal wave regime, with peak velocities occurring at high and low tide [32]. The M_2 tidal constituent is dominant, with a period of approximately 12.42 hours [33]. The strong semi-diurnal tides drives a range of approximately 1.6–5m from mean neap to mean spring, current speeds exceeding 3ms^{-1} and zones of high turbulence [34].

3. Methodology

This study employs a combination of measured and modelled data for the analysis of hydrodynamics in and around Ramsey Sound. Post-processed acoustic Doppler current profiler (ADCP) data provides an accurate indication of 3D flow conditions across specific areas of interest. Measured data is then used to calibrate a 2D depth-averaged hydrodynamic model of the entire Ramsey Sound and surrounding waters. In turn, the hydrodynamic model provides further insight into near- and far-field hydrodynamics of its flow regime over a larger temporal scale.

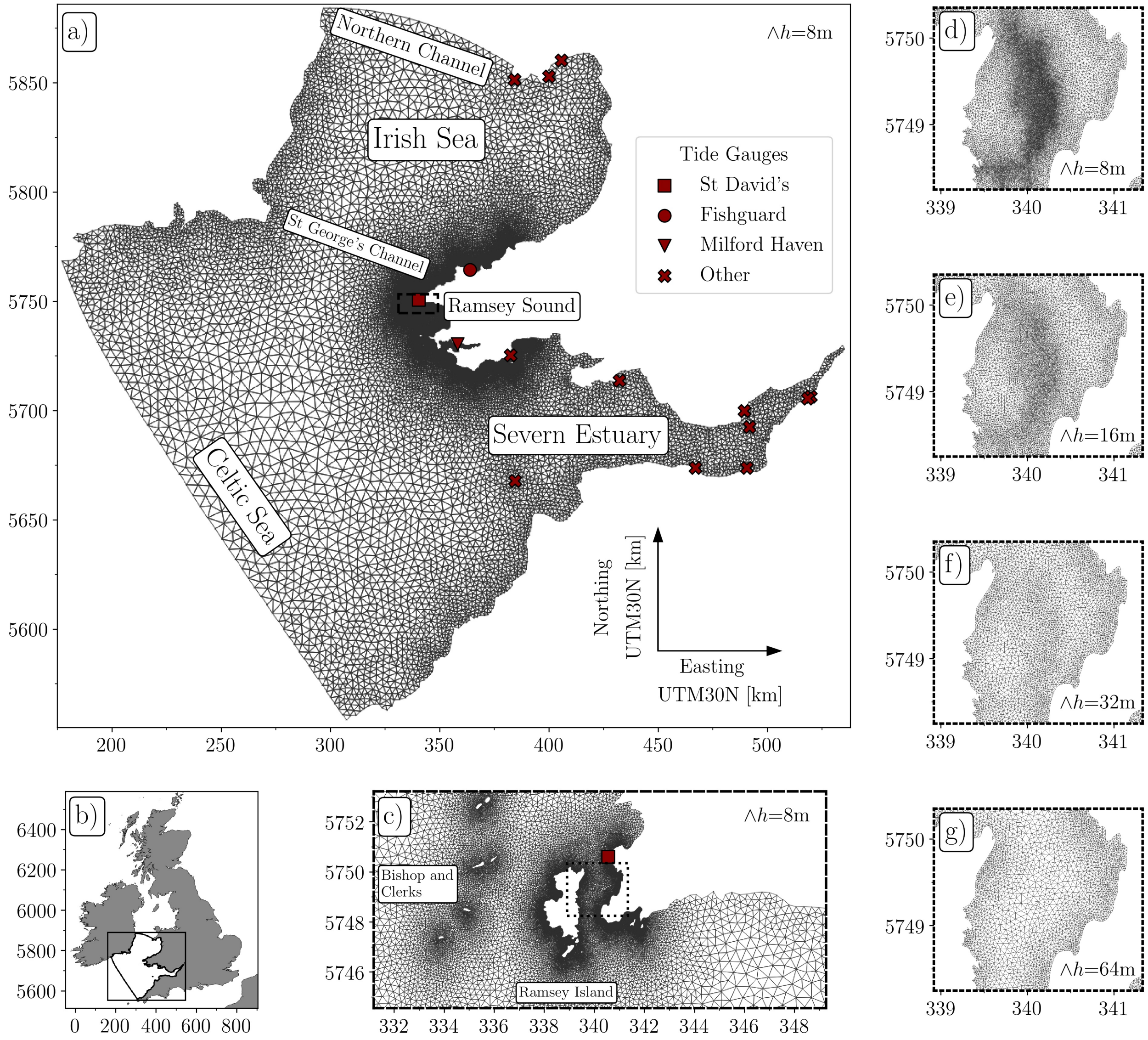

Figure 1: Domain and computational mesh for Ramsey Sound and surrounding seas. Mesh element size ranges between a maximum of 8km in the open ocean, 1km/300m at coastlines outside/inside of Pembrokeshire, 50m around small islands and 25m around Ramsey Sound. Minimum mesh element size $\wedge h$, applied to areas exhibiting high bathymetry gradients in and around Ramsey Sound, is set to $\wedge h$=8m in frames a), c), d), with the effect on wake recovery when applying e) $\wedge h$=16m, f) $\wedge h$=32m and g) $\wedge h$=64m assessed in this study. Also indicated are tide gauge locations [30] used for tide constituent validation in the model.

3.1. 2D hydrodynamic modelling

Thetis (`http://thetisproject.org/`) is a 2-D/3-D flow solver for simulating coastal and estuarine flows implemented using the *Firedrake* finite element Partial Differential Equation (PDE) solver framework [22, 35, 36]. Considered in this work are the non-conservative form of the nonlinear shallow water equations:

$$\frac{\partial \eta}{\partial t} + \nabla \cdot (H_d \tilde{\mathbf{u}}) = 0, \tag{1}$$

$$\frac{\partial \tilde{\mathbf{u}}}{\partial t} + \tilde{\mathbf{u}} \cdot \nabla \tilde{\mathbf{u}} - \nu \nabla^2 \tilde{\mathbf{u}} + f \tilde{\mathbf{u}}^{\perp} + g \nabla \eta = -\frac{\tau_b}{\rho H_d}, \tag{2}$$

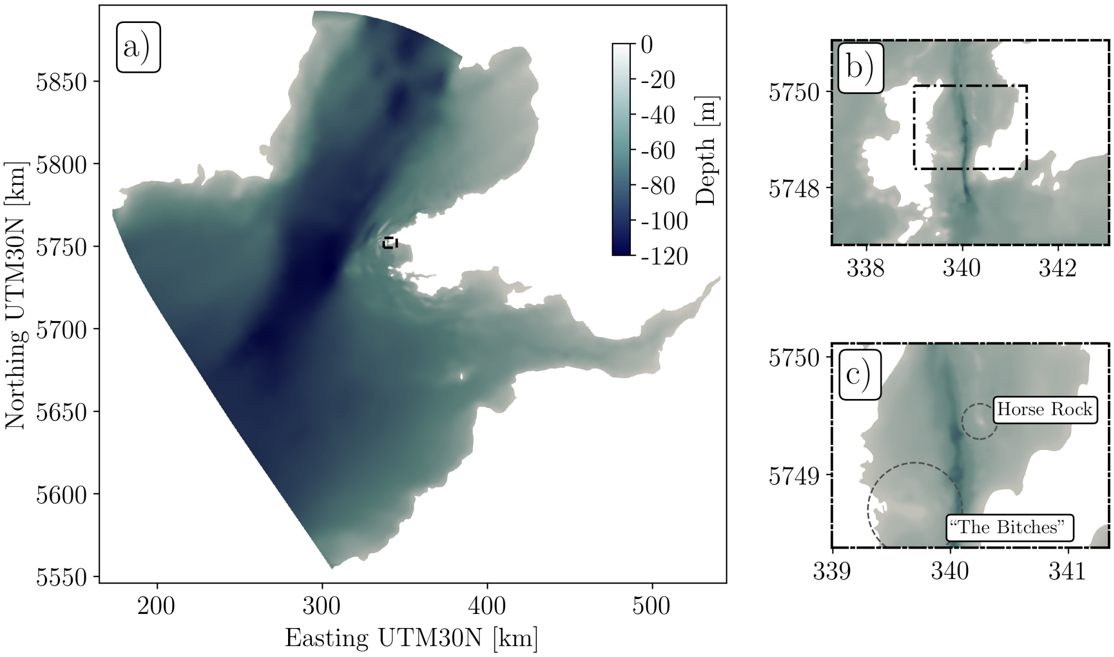

Figure 2: Bathymetry data within the model domain interpolated onto the computational mesh, corrected to Mean Sea Level (MSL) (m). Magnified areas indicate Ramsey Sound and identify Horse Rock and "The Bitches". The north-south trench can also be observed down the centre-line of the entire channel.

$$\frac{\tau_b}{\rho} = gn^2 \frac{|\tilde{\mathbf{u}}|\tilde{\mathbf{u}}}{H_d^{\frac{1}{3}}}, \tag{3}$$

where η is the water elevation, H_d is the total water depth, ν is the kinematic viscosity of the fluid and $\tilde{\mathbf{u}}$ the depth-averaged velocity vector with horizontal components $\tilde{u}$ and $\tilde{v}$ depicting easterly and northerly flow, respectively. The term $f\tilde{\mathbf{u}}^{\perp}$ represents the Coriolis "force", where $\tilde{\mathbf{u}}^{\perp}$ is the velocity vector rotated counter-clockwise over 90° and $f = 2\Omega\sin(\zeta)$, in which Ω is the angular frequency of the Earth's rotation and ζ is latitude. Seabed roughness effects are represented using Manning's formulation (3) for bed shear stress (τ_b), using the Manning coefficient n (sm$^{-1/3}$). Intertidal processes are treated using the wetting and drying formulation detailed in Kärnä et al. [37].

3.1.1. Model setup

The model itself is configured similarly to other tidal resource characterisation studies which apply *Thetis* [38, 39, 40, 41]. A discontinuous Galerkin finite element spatial discretisation (DG-FEM) is utilised through the choice of a $P_{1DG} - P_{1DG}$ velocity-pressure finite element pair. A semi-implicit Crank-Nicolson timestepping approach is applied. The nonlinear discretised shallow water equations are iteratively solved with Newton's algorithm using the PETSc library [42].

3.1.2. Computational domain

The mesh generation framework *qmesh* (`https://www.qmesh.org/`, [43]), which applies the meshing tool *Gmsh* [44], is used to produce unstructured meshes to represent the domain, spanning a large section of the Irish Sea and encompassing parts of the Celtic Sea and Northern Channel, as indicated in Fig. 1a. A finer resolution is applied along the coastlines to capture intertidal processes [37]. The mesh is further refined around bathymetric features in Ramsey Sound of interest to this study (Fig. 1d). Here, a minimum mesh element size of $\wedge h$=8m is applied, an appropriate size as indicated by a Ramsey Sound study by Haverson et al. [17] which implemented $\wedge h$=10m in these areas. The effect of increasing the minimum mesh element length in these areas to $\wedge h$=16m, $\wedge h$=32m and $\wedge h$=64m, as indicated in Fig. 1e–g, is later modelled and discussed.

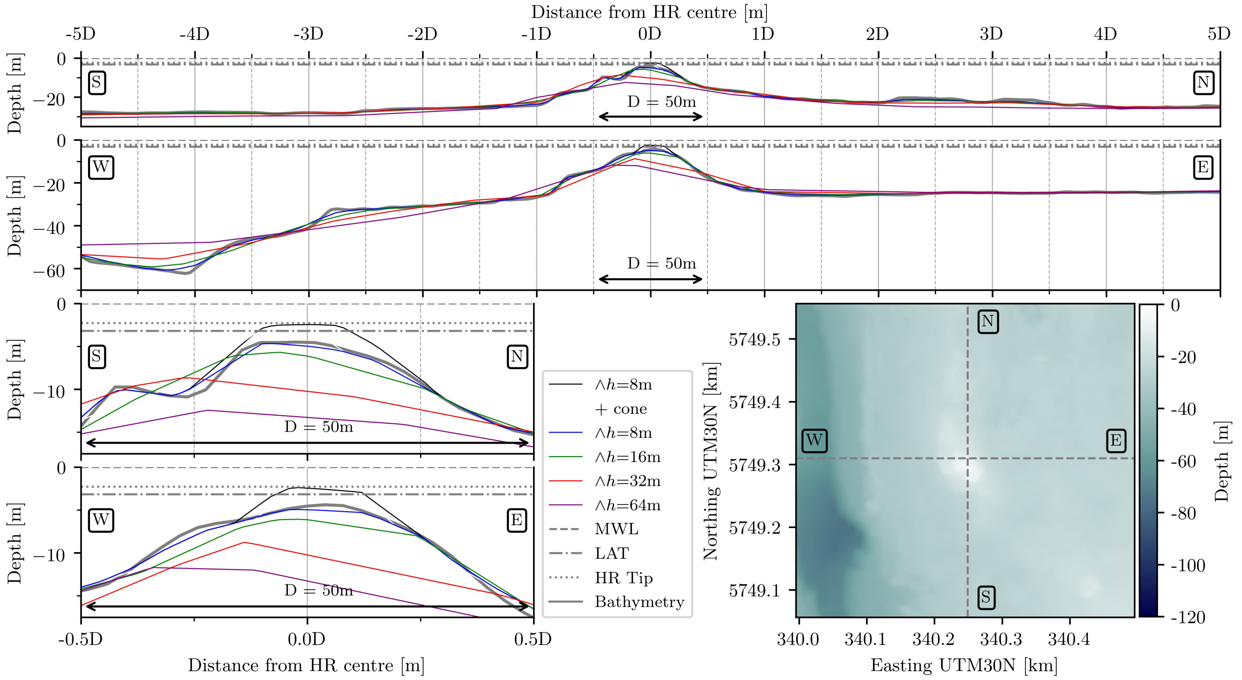

Figure 3: Horse Rock bathymetry according to data from the Hydrographic Office (HO), including South-North (S–N) and West-East (W–E) cross-sections (top two frames respectively, with corresponding zooms bottom-left). Interpolation of bathymetry onto meshes with different minimum mesh element lengths ($\wedge h$) is indicated, including the implementation of a conical structure (the thin black line identified with $\wedge h$ = 8m + cone) to increase the height of Horse Rock to +0.9m Lowest Astronomical Tide (LAT). Depth is relative to MSL, corrected from LAT.

3.1.3. Bathymetry and forcing

The bathymetry data used in the hydrodynamic model is comprised of multiple datasets. Data for the majority of the domain is obtained from the Edina Digimap Service at a resolution of 1 arc second (ranging from 18m to 20m in the model domain) where possible and 6 arc seconds (111m to 119m) otherwise [45]. An 11 × 12km rectangle around Ramsey Sound is covered by 2m resolution bathymetry data from the UK Hydrographic Office (UKHO) [46]. All bathymetry data is configured to the UTM zone 30N projection. Converting all the datasets from LAT (Lowest Astronomical Tide) to MSL in the z-direction made use of tide constituent data (Q_1, O_1, P_1, K_1, N_2, M_2, S_2, K_2) from the TPXO database [47]. An overview of the bathymetry field applied in the model is given on Fig. 2. In addition, the TPXO database is also used to force the model at the ocean boundaries [47]. Tidal forcing is the primary model component which aligns the model to a specific moment in time.

In this study, particular attention is paid to the characterisation and representation of Horse Rock. Notable discrepancies occur between representation of this feature in the 2m resolution UKHO dataset and other accounts [48]. In particular, the UKHO data indicates that Horse Rock does not pierce the water surface, with the tip reaching -1.21m LAT. Admiralty Charts indicate a depth of +0.9m LAT [31], suggesting drying at spring tide lows which is also observed in video footage of the area [48]. As the bathymetry data from the UKHO was measured on a vessel, it is likely that capturing the tip of Horse Rock would not have been possible. The tip of Horse Rock is therefore raised to +0.9m LAT by incorporating an artificial conical feature on the top. Furthermore, a smoothing function applied to the bathymetry field to increase stability is not implemented around Horse Rock, in order to preserve its overall height and structure. Fig. 3 demonstrates how the bathymetry used in different versions of the numerical model set-up represent Horse Rock, based on mesh resolution and the implementation of the conical pinnacle.

3.1.4. Representation of bed shear stress

In the process of calibrating the numerical model, the validity of implementing a constant seabed friction parameter across the domain, as is often applied in similar studies [11, 17], is investigated. Thiébot et al. [29] and Guillou and Chapalain [28] both acknowledge the heterogeneous nature of bottom sediments in hydrodynamic modelling of sediment transport in the English Channel, the former in an investigation of the effect of tidal turbines. Data is sourced from the British Geological Survey (BGS) to inform the model regarding bed classification and therefore grain size d_{50} in mm [49] across the domain. Coastal areas where data is unavailable is estimated to have grain size d_{50}=6mm, equivalent to 'small gravel'. In determining a relationship between bed classification and Manning coefficient n (Table 1), the Nikuradse parameter for sand grain roughness is calculated through $k_s = 2.5d_{50}$, from which roughness length z_0 in m (the height above the seabed where fluid velocity is zero) can be determined with $z_0 = \frac{k_s}{30}$ and thus Manning coefficient with $n = 0.04\sqrt[6]{k_s}$ [50]. Fig. 4a–b shows the spatial application of the variable Manning coefficient field, denoted as N. Scaling of N is used as a tuning parameter in the calibration process, as either a constant scaling applied throughout the domain (e.g. $1.25N$), or as a scale factor applied locally in the area of interest (e.g. $1.25N^*$ in Fig. 4c).

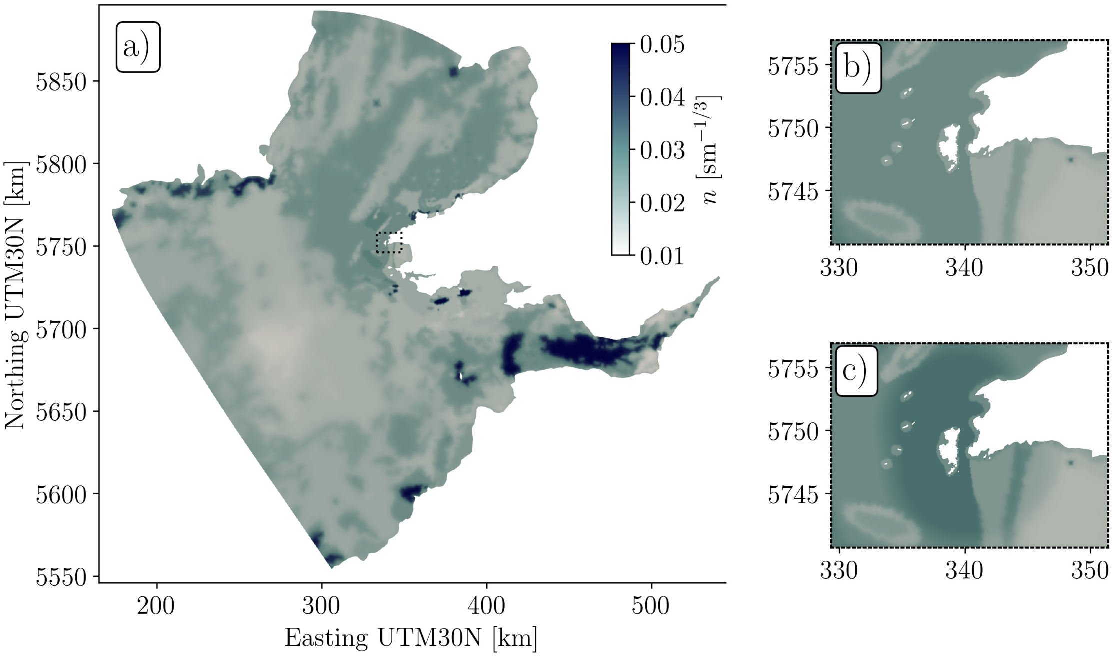

Figure 4: Manning n coefficient calculated using data from the British Geological Survey interpolated as a variable field denoted by N onto computational mesh domain. c) indicates variable scaling field N^*, with Manning coefficient amplified locally to Ramsey Sound at a radius of 10km from Horse Rock, converging towards N over a further 2km.

Table 1: Data utilised in calculating roughness length z_0 and Manning coefficient n from British Geological Survey data on bed classification and associated grain size d_{50}.

Bed classification	d_{50} (mm)	z_0 (mm)	n (sm$^{-1/3}$)
Bedrock	$768 \geq d_{50} > 2048$	$64 \geq z_0 > 170.667$	$0.045 \geq n > 0.053$
Boulder	$256 \geq d_{50} > 768$	$21.333 \geq z_0 > 64$	$0.037 \geq n > 0.045$
Cobble	$64 \geq d_{50} > 256$	$5.333 \geq z_0 > 21.333$	$0.029 \geq n > 0.037$
Very coarse gravel	$32 \geq d_{50} > 64$	$2.667 \geq z_0 > 5.333$	$0.026 \geq n > 0.029$
Coarse gravel	$16 \geq d_{50} > 32$	$1.333 \geq z_0 > 2.667$	$0.023 \geq n > 0.026$
Medium gravel	$8 \geq d_{50} > 16$	$0.667 \geq z_0 > 1.333$	$0.021 \geq n > 0.023$
Fine gravel	$4 \geq d_{50} > 8$	$0.333 \geq z_0 > 0.667$	$0.019 \geq n > 0.021$
Very coarse sand	$2 \geq d_{50} > 4$	$0.167 \geq z_0 > 0.333$	$0.017 \geq n > 0.019$
Coarse sand	$1 \geq d_{50} > 2$	$0.083 \geq z_0 > 0.167$	$0.015 \geq n > 0.017$
Medium sand	$0.5 \geq d_{50} > 1$	$0.042 \geq z_0 > 0.083$	$0.013 \geq n > 0.015$
Fine sand	$0.25 \geq d_{50} > 0.5$	$0.021 \geq z_0 > 0.042$	$0.012 \geq n > 0.013$
Very fine sand	$0.125 \geq d_{50} > 0.25$	$0.010 \geq z_0 > 0.021$	$0.010 \geq n > 0.012$
Silt, clay, mud	$0.0625 \geq d_{50} > 0.125$	$0.005 \geq z_0 > 0.01$	$0.009 \geq n > 0.010$

3.2. Measured data

Measured velocity and water depth data provides both a snapshot of hydrodynamic conditions within Ramsey Sound, and a visual and numerical basis upon which the model calibration process can be based. Two ADCP survey datasets support this study [14, 17]. Vessel-mounted ADCP survey data provides a spatially variable representation of tidal conditions in Ramsey Sound. To complement this, a single seabed-mounted ADCP dataset provides time series data at a fixed location.

3.2.1. Data acquisition

A four-beam 600-kHz broadband Workhorse Sentinel ADCP unit, manufactured by Teledyne RD Instruments and gunwhale-mounted on Cardiff University's research vessel, *Guiding Light*, was used to conduct surveys across the central portion of Ramsey Sound (Fig. 5). Evans et al. [14] describes the process and challenges encountered when obtaining the data over a set of six transects. Transects T1–T3 are surveyed downstream (to the north) of Horse Rock on the flood tide and transects T4–T6 downstream (to the south) of Horse Rock on the ebb tide, indicating northerly and southerly flow, respectively. The downstream distance from the idealised transects to Horse Rock varied between 50 m (T3 and T4), 250 m (T2 and T5), and 400 m (T1 and T6) [14]. The selected days (01 June 2012 for flood tide readings T1–T3 in nine continuous circuits and 02 June 2012 for ebb tide readings T4–T6 in eight continuous circuits) of the survey lie approximately half way between spring and neap tide in the area.

Fixed-position velocity data was obtained from a 600-kHz Workhorse Sentinel deployed on the seabed in the north-western portion of Ramsey Sound [51], as indicated in Fig. 5. The instrument sampled at a rate of 1Hz (1s), recording and averaging data at 10 minute intervals (i.e. averaging 600 samples) between 18 February 2009 – 21 March 2009.

3.2.2. Interpretation of data for model validation

Sub-sampling of the ADCP boat data was performed in order to validate the numerical model as the model timestep, Δt, is much greater than the time difference between ADCP readings. Easterly (u) and northerly (v) ADCP velocity data are depth-averaged to $\tilde{u}$ and $\tilde{v}$ over the water column and time-averaged to $\tilde{u}_{10}$ and $\tilde{v}_{10}$, the subscript donating the time-averaging window in seconds. A 10 second time-averaging window is deemed appropriate in acknowledging both the spatial and temporal variance of the ADCP data. The numerical model is then configured to run for the duration of the vessel-mounted ADCP survey. Noticeable volatility exists in the exact path of each boat journey along individual transects (Fig. 5), with navigation

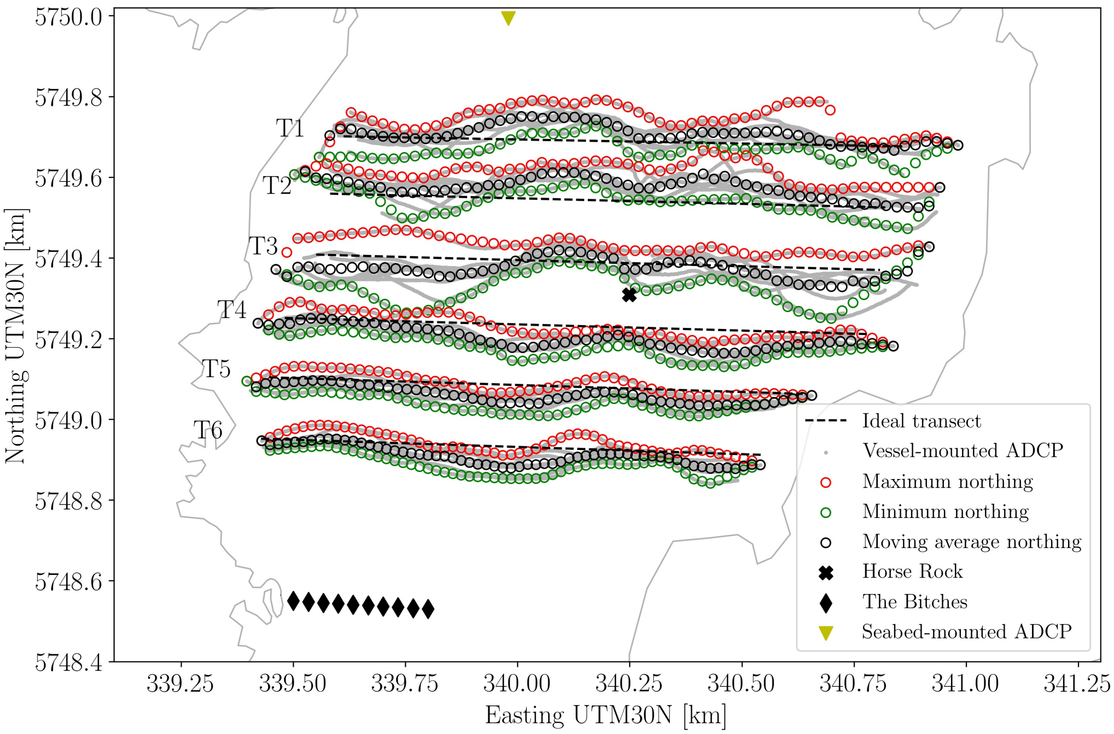

Figure 5: Model data sampling locations are established upon navigation of the ADCP vessel. Along each idealised transect, maximum, minimum and average northing values are determined based on evenly spaced easting bins. Easting coordiantes indicate the centre-point of these bins. ADCP data at transects T1 to T3 was collected as the tide ebbed, and transects T4 to T6 as the tide flooded.

being complicated by the high current conditions. The average R^2 correlation coefficient between reading locations on each boat journey and the ideal transect is 0.349. Therefore, to reduce the number of required model detector (i.e. virtual gauge/ADCP) locations when validating the model against individual ADCP boat journeys, a data envelope of all the ship-mounted ADCP reading coordinates is generated. Along each transect, all boat journey readings are ordered from west to east, with maxima, minima and averages of the boat's northing positions computed within 50 evenly distributed easting bins. In total, this leads to 150 coordinates $(x,\ y)$ being generated for each transect, by combining easting bin mid-points (x) with corresponding maximum, minimum and average northing points (y). The numerical models are set up to extract a time-series of elevation η and depth-averaged velocity components $\tilde{u}$,$\tilde{v}$ for the duration of the simulation at each timestep. ADCP $\tilde{u}_{10}$ and $\tilde{v}_{10}$ are sub-sampled to match the timestepping of the numerical model. Depth-averaged velocity data at the model detector locations positioned closest to the sub-sampled ADCP dataset are then utilised for validation.

4. Results

4.1. Numerical model calibration

Calibrating the model against a comprehensive field dataset permits investigation of the effectiveness of 2D modelling in characterising the hydrodynamics surrounding small-scale, submerged bathymetric obstructions. Model depth-averaged velocity components $\tilde{u}$ and $\tilde{v}$ are extracted and resolved to calculate the magnitude vector $|\tilde{\mathbf{u}}|$, and free-surface elevation η to compare values in corresponding locations and times covered by the measured data. A sensitivity study is performed by adjusting the representation of physical characteristics in the model. A key focus of this research is highlighting common simplifications in 2D resource characterisation studies that may distort the influence of complex features in Ramsey Sound, and other locations that exhibit similar geographical features. The computational mesh comprises a minimum element size of $\wedge h$=8m around bathymetric features in Ramsey Sound so as to minimise smoothing effects that arise from interpolating bathymetry onto a coarser mesh. The effect of increasing $\wedge h$ is explored later in the results. Furthermore, a conical structure is added to the tip of Horse Rock to better match the depth of +0.9m LAT observed in Admiralty Charts [31]. First the process of tuning the representation of seabed roughness is demonstrated, comparing scaled implementations of variable Manning coefficient fields N and N^* (Fig. 4a–c) with constant values.

The open boundaries of the unstructured mesh domain extend far beyond Ramsey Sound. As such, validation begins by looking beyond the immediate areas of interest. The model simulates the tidal conditions for 30 days between 27 October 2019 to 26 November 2019, sufficient time to represent a full lunar month and harmonically analyse the free-surface elevation η and extract the principal tidal constituents from the model at specific locations where field observations are available. Following timestep sensitivity analyses, a value of Δt=100s is deemed appropriate for temporal discretisation, whilst time-averaging of the modelled outputs is considered unnecessary. Fig. 6 shows a comparison between M_2 and S_2 amplitude α and phase ϕ for the numerical model applying different Manning coefficient fields and equivalent data provided by the British Oceanographic Data Centre (BODC) [30], at locations indicated in Fig. 1a.

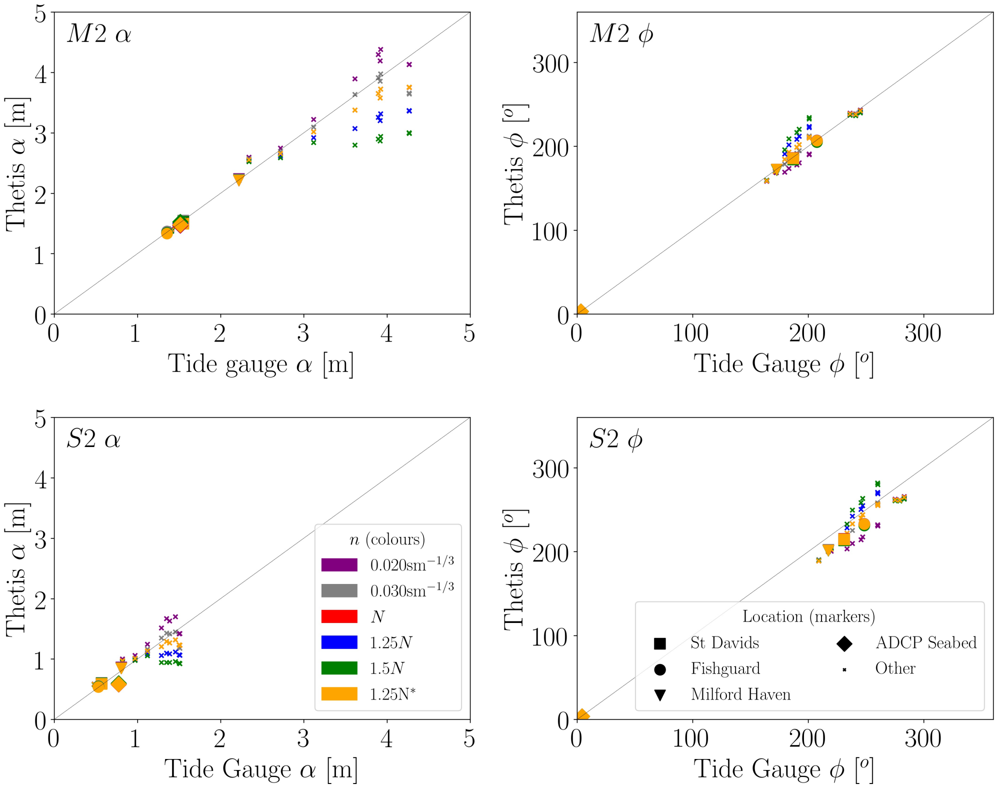

Figure 6: Comparing modelled and measured M_2 and S_2 tidal constituent amplitude α and phase ϕ at tide gauge locations for different Manning coefficient fields. The near identical values between N and $1.25N^*$ obscure results for N. Tide gauge locations are indicated in Fig. 1a.

Manning coefficient field test cases in Ramsey Sound itself are then studied. Validation against the seabed-mounted ADCP survey data permits comparisons over multiple tidal cycles, informing adjustments

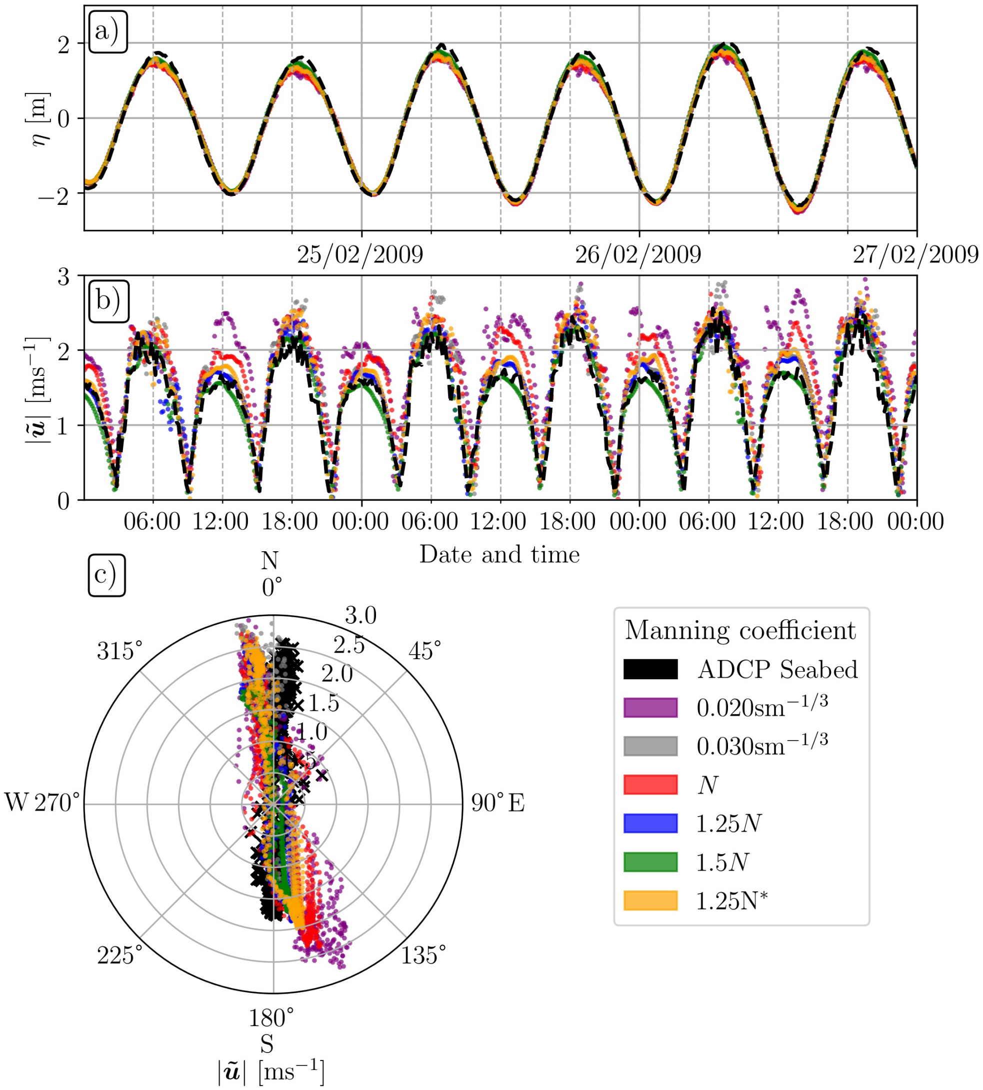

Figure 7: Seabed-mounted ADCP elevation a) η and b, c) depth-averaged velocity $\tilde{\mathbf{u}}$ measurements (see Fig. 5 for sample location) and *Thetis* model. Data collected during a spring tide over four tidal cycles and displayed as a, b) time-series and c) a polar plot.

in indicating prediction variations at a fixed location (indicated on Fig. 5) to a high precision and over a large temporal scale. Fig. 7 presents three days (roughly six tidal cycles) at spring tide, from 00:00 24 February 2009 to 15:20 27 February 2009, with a timestep of Δt=100s. Model and measured data is compared for elevation η (panel a), depth-averaged velocity magnitude $|\tilde{\mathbf{u}}|$ (b, c) and flow direction θ (c).

Comparing model outputs of depth-averaged velocity (easterly $\tilde{u}$, northerly $\tilde{v}$ and magnitude $|\tilde{\mathbf{u}}|$) to depth- and time-averaged data from the vessel-mounted ADCP survey ($\tilde{u}_{10}$, $\tilde{v}_{10}$ and $|\tilde{\mathbf{u}}_{10}|$) allows a more comprehensive view of flow magnitude and direction across the study area. A Δt=50s timestep is implemented to provide a higher spatial alignment between measured and modelled data sampled as per the methodology outlined in Section 3.2.2. A sensitivity analysis concluded that the difference in output between identical models implementing Δt=50s and Δt=100s was negligible. Fig. 8 displays a comparison of maximum model $|\tilde{\mathbf{u}}|$ and ADCP $|\tilde{\mathbf{u}}_{10}|$ data over sequential boat journeys in a time series, and the corresponding R^2 correlation coefficient. The plots indicate the ability of the different models to characterise changing flow conditions

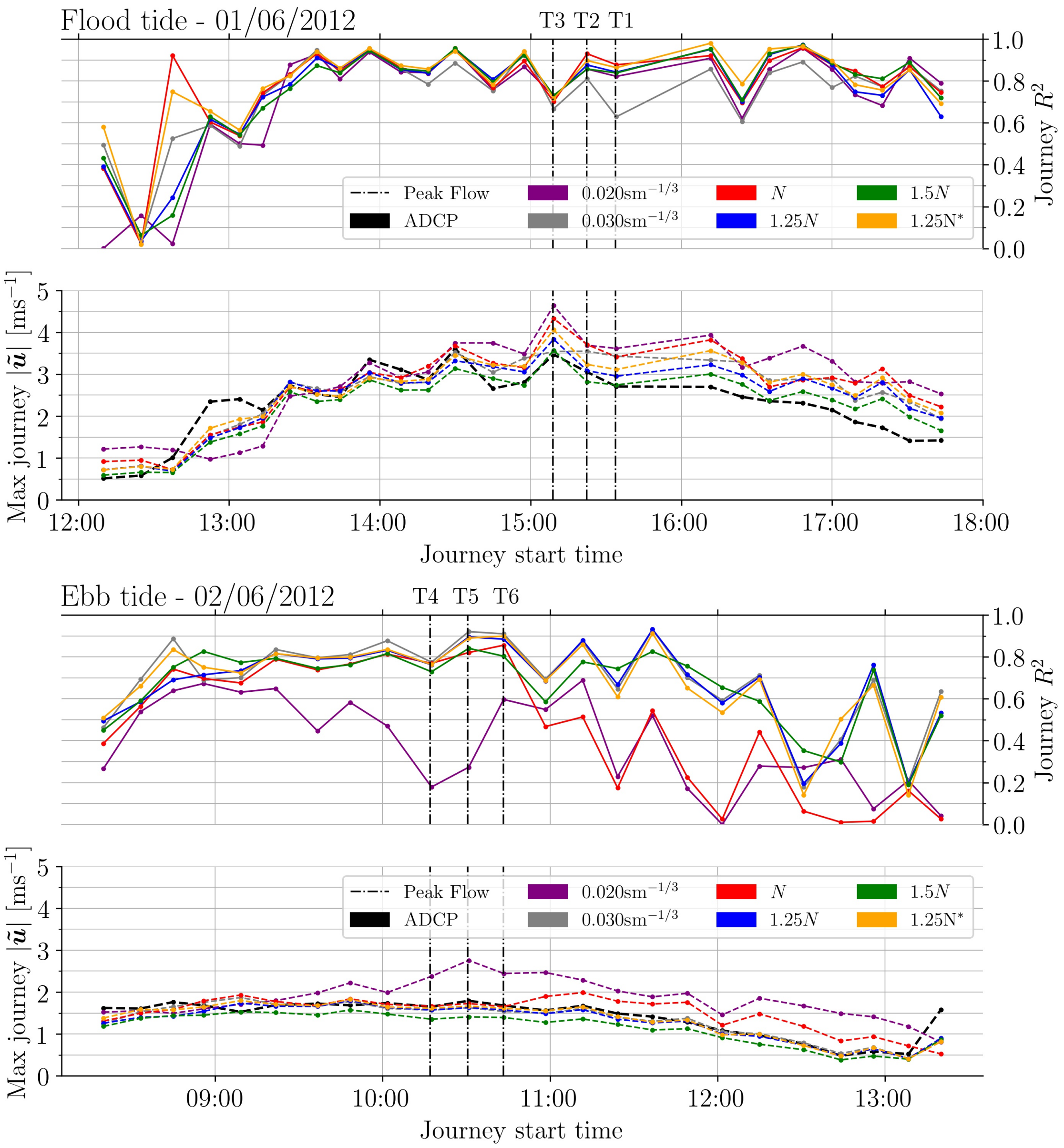

Figure 8: Maximum time- and depth-averaged velocity magnitude $|\tilde{\mathbf{u}}|_{10}$ from individual boat journeys in vessel-mounted ADCP survey and equivalent $|\tilde{\mathbf{u}}|$ data sampled from numerical models. R^2 correlation coefficient between ADCP and model data for each journey is also indicated.

for the duration of the ADCP surveys. Fig. 9 illustrates modelled $|\tilde{\mathbf{u}}|$ and measured $|\tilde{\mathbf{u}}_{10}|$ during peak ebb and flood (as displayed on Fig. 8), as well as the sampling locations. Here, model validation is represented spatially, indicating areas of the domain better able to capture peak flow conditions in Ramsey Sound.

Model configurations are analysed numerically to supplement visual comparisons. Table 2 indicates R^2 correlation coefficient and root mean squared error (RMSE) of model configurations against the measured datasets. The different timescales and spatial extents afforded by the measured data provides a comprehensive overview of the effect of the Manning coefficient on model calibration. Additionally, the results serve as an indicator of which field affords the best representation of the hydrodynamics in Ramsey Sound by the numerical model.

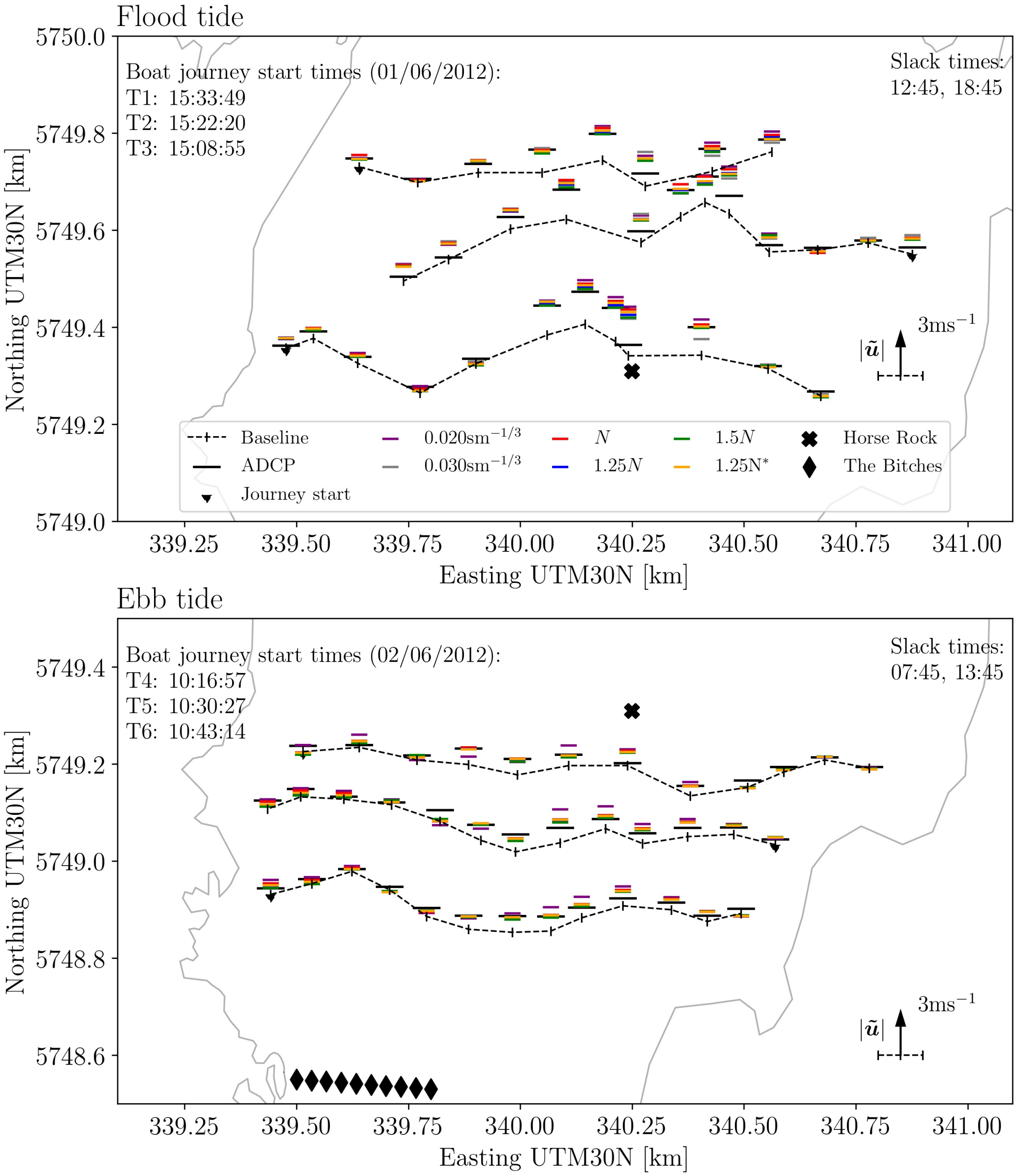

Figure 9: Comparison of depth-averaged velocity magnitude between the numerical model $\tilde{\mathbf{u}}$ (implementing different Manning coefficient fields) against equivalent 10s time-averaged vessel-mounted ADCP survey data $|\tilde{\mathbf{u}}_{10}|$ during peak ebb and flood flows (as indicated on Fig. 8). Vertical distance of ADCP and model data from the baseline (also sample location) indicates velocity magnitude.

It can be observed that elevation is well calibrated in all configurations of the model, with low errors observed in tidal constituent amplitude α and phase ϕ (Fig. 6) and elevation η in the seabed-mounted ADCP data (Fig. 7a). Scaled configurations of the variable Manning coefficient field (1.25N and 1.5N) skew model constituent data from the measured equivalents due to the magnification of areas of high seabed friction far-field from Ramsey Sound, particularly in the Severn Estuary, a sensitive area due to resonance characteristics.

The Manning coefficient distribution fields $1.25N$ and $1.5N$ exhibit the best fit with the seabed ADCP data in terms of depth-averaged easterly ($\tilde{u}$), northerly ($\tilde{v}$) and magnitude ($|\tilde{\mathbf{u}}|$) velocities. Relative errors between model configurations against the boat-mounted ADCP dataset indicate notable dissimilarities, with results obtained using the constant Manning coefficient $0.02\text{sm}^{-1/3}$ and the variable N exhibiting the largest discrepancies from the measured data (Fig. 8 and 9). In general, $\tilde{u}$ velocity validation is quite poor across all models, with improved calibration observed for $\tilde{v}$, $|\tilde{\mathbf{u}}|$ and θ, indicating the dominance of $\tilde{v}$ in the $|\tilde{\mathbf{u}}|$ vector. A diagnosis of these trends is provided in the discussion. Upon completing the validation process, it was deemed that a Manning coefficient field of $1.25N^*$ offered, overall, the best fit with measured data. The range in seabed composition characterised by the variable field based on BGS data, combined with further scaling solely in the vicinity of Ramsey Sound, provides a favourable balance of agreement with observational data throughout the whole domain.

Table 2: R^2 correlation coefficient and Root Mean Squared Error (RMSE) of *Thetis* model outputs against tide gauge constituent data (Fig. 6), and seabed- (Fig. 7) and vessel-mounted (Figs. 8 and 9) ADCP survey data. Indicated units are for RMSE only (R^2 is dimensionless). Bold readings indicate model exhibiting most favourable correlation or error.

	R^2						RMSE					
Tide gauges	0.02	0.03	N	$1.25N$	$1.5N$	$1.25N^*$	0.02	0.03	N	$1.25N$	$1.5N$	$1.25N^*$
M_2 α (m)	0.98	0.97	**0.99**	0.97	0.91	**0.99**	**0.20**	0.23	0.23	0.45	0.66	0.23
M_2 ϕ $(^o)$	**0.99**	**0.99**	**0.99**	0.96	0.93	**0.99**	6.93	**4.47**	5.83	11.91	17.08	5.82
S_2 α (m)	0.91	0.87	**0.92**	0.84	0.67	**0.92**	0.16	0.14	**0.13**	0.22	0.30	**0.13**
S_2 ϕ $(^o)$	**0.99**	**0.99**	**0.99**	0.97	0.94	**0.99**	22.01	14.14	**13.19**	13.60	16.14	13.21
Seabed ADCP	0.02	0.03	N	$1.25N$	$1.5N$	$1.25N^*$	0.02	0.03	N	$1.25N$	$1.5N$	$1.25N^*$
$\tilde{u}$ (ms^{-1})	0.10	0.12	0.10	0.15	**0.19**	0.12	0.59	0.35	0.46	0.34	**0.29**	0.35
$\tilde{v}$ (ms^{-1})	0.94	0.98	0.97	**0.99**	**0.99**	0.98	0.55	0.34	0.40	0.21	**0.18**	0.27
$|\tilde{\mathbf{u}}|$ (ms^{-1})	0.65	0.85	0.83	**0.93**	**0.93**	0.90	0.60	0.32	0.40	0.21	**0.16**	0.27
θ $(^o)$	0.91	0.94	0.92	**0.97**	**0.97**	0.96	38.09	32.07	35.10	25.21	**22.31**	26.45
η (m)	**0.99**	**0.99**	**0.99**	**0.99**	**0.99**	**0.99**	0.18	**0.12**	0.17	0.14	**0.12**	0.15
Boat ADCP: Flood	0.02	0.03	N	$1.25N$	$1.5N$	$1.25N^*$	0.02	0.03	N	$1.25N$	$1.5N$	$1.25N^*$
$\tilde{u}$ (ms^{-1})	0.21	0.11	**0.24**	0.16	0.20	0.18	0.27	0.34	0.25	0.29	**0.24**	0.27
$\tilde{v}$ (ms^{-1})	0.75	0.82	0.83	**0.85**	**0.85**	**0.85**	0.77	0.53	0.61	0.51	**0.45**	0.52
$|\tilde{\mathbf{u}}|$ (ms^{-1})	0.71	0.77	0.79	0.81	**0.82**	**0.82**	0.69	0.49	0.55	0.46	**0.40**	0.47
θ $(^o)$	0.83	0.92	0.92	0.91	0.92	**0.93**	65.97	42.79	43.35	44.69	43.35	**41.18**
Boat ADCP: Ebb	0.02	0.03	N	$1.25N$	$1.5N$	$1.25N^*$	0.02	0.03	N	$1.25N$	$1.5N$	$1.25N^*$
$\tilde{u}$ (ms^{-1})	0.21	**0.54**	0.40	0.52	0.48	0.52	0.29	**0.13**	0.19	0.14	**0.13**	0.14
$\tilde{v}$ (ms^{-1})	0.60	0.88	0.74	0.88	**0.90**	0.87	0.61	**0.25**	0.42	**0.25**	**0.25**	0.26
$|\tilde{\mathbf{u}}|$ (ms^{-1})	0.32	**0.77**	0.54	0.76	0.75	0.76	0.56	**0.23**	0.37	**0.23**	**0.23**	0.24
θ $(^o)$	0.71	0.86	0.77	**0.87**	0.85	0.86	51.54	31.41	44.44	**31.02**	31.94	32.81

4.2. Wake characteristics

Hydrodynamics in Ramsey Sound are analysed over a spring-neap tidal cycle, with particular focus on the wake generated by Horse Rock. Both measured and modelled data are investigated, providing a comprehensive representation of flow conditions.

4.2.1. ADCP data

ADCP surveys in Ramsey Sound provide a snapshot of hydrodynamic features that may be otherwise obscured or misrepresented by numerical modelling assumptions. Furthermore, analysis of measured data offers a route for the potential diagnosis of deviations between observed and modelled results. Highlighted trends from the ADCP datasets in this section have been noted in previous literature [14, 52, 53]. Recalling the seabed-mounted ADCP readings in Fig. 7b, the site's tidal asymmetry is apparent, with flood tide flow being almost 50% greater than the subsequent ebb flow. The dominant currents travel almost rectilinearly, with flood and ebb headings of 5° and 180°, respectively. It can also be observed that peak flood and ebb velocities coincide with high and low tide, respectively, characteristics consistent with previous research indicating that Ramsey Sound experiences a progressive tidal wave [32]. Therefore, Horse Rock dries during peak ebb currents around spring tides, which coincides with low water.

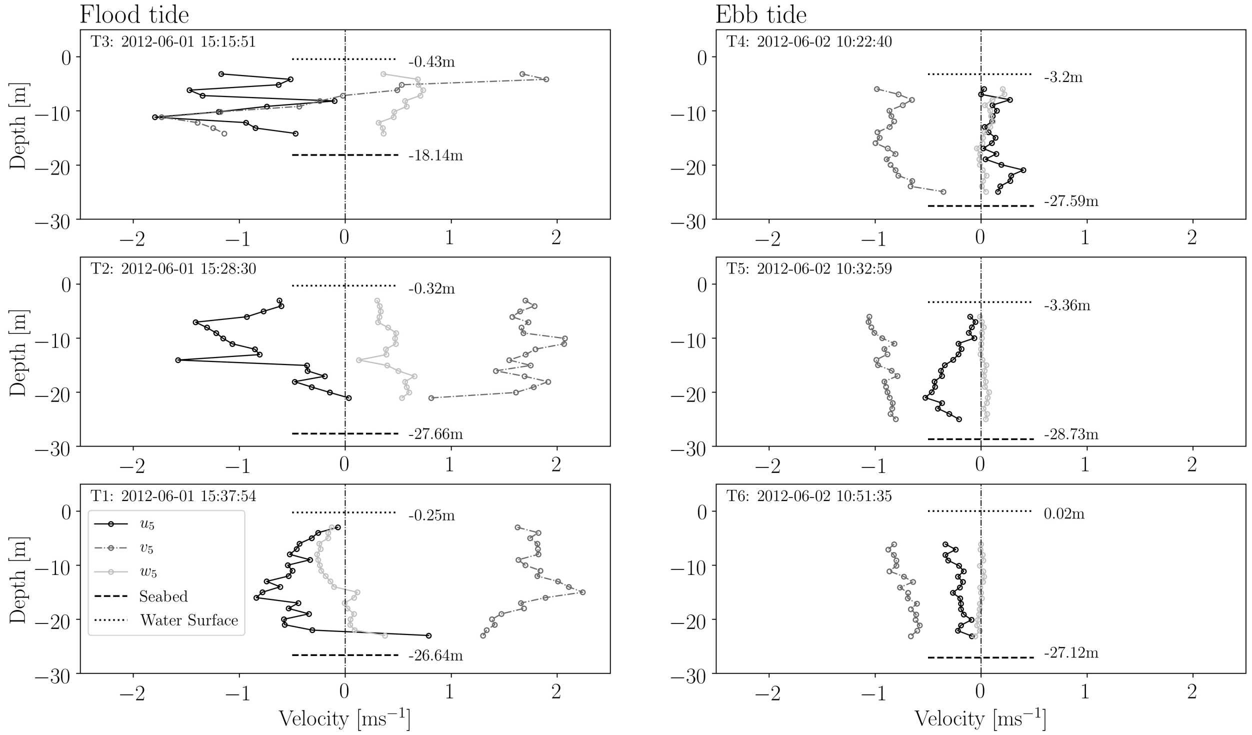

Figure 10: Vertical profiles of time-averaged velocity components (u_5, v_5 and w_5) from the vessel-mounted ADCP surveys along the stream-wise centre line of Horse Rock during peak flood and ebb tides. Depth is relative to mean water level (MWL).

In analysing 3D velocity data (u, v and w) from the vessel-mounted ADCP survey, a sliding 5 second time averaging window (u_5, v_5 and w_5) is applied. A lower averaging window is applied than during the model validation stages as to conserve water column structure. Data along the stream-wise centre line of Horse Rock is extracted from peak ebb and flood flow for each transect (as in Fig. 9), and presented in Fig. 10. Water elevation data is derived from the seabed-mounted ADCP survey, which is harmonically reconstructed to the displayed timestamps of the vessel-mounted ADCP readings. Flood tide readings indicate relatively complex flow immediately downstream from Horse Rock (T3), with northward velocity v_5 reversals occurring through the water column. The wake recovery structure can be perceived through a rise and fall of eastward velocity u_5 further downstream (T2 and T1, respectively). Vertical velocity w_5 also decreases towards 0ms^{-1}, signalling a gradual return from upwelling to quasi-2D flow. Meanwhile, readings on the ebb tide indicate relatively consistent v_5 and w_5 values between transects, and predominantly quasi-2D flow throughout. The slight wake structure is illustrated in the reversal of u_5 between T4 and T5, suggesting a shorter wake recovery distance than during the flood tide.

4.2.2. Hydrodynamic model data

The configuration of a depth-averaged hydrodynamic model significantly increases the spatial and temporal extent in which wake characteristics in Ramsey Sound can be investigated, in comparison to direct analysis of the ADCP surveys alone. The following section outlines observations that can be made from model outputs, and explores how mesh resolution can affect the predicted hydrodynamic structures.

Following calibration of the numerical model, a full spring-neap tidal cycle from 29 October 2019 to 28 November 2019 is considered, applying a timestep size of Δt=100 seconds. Fig. 11 displays depth-averaged velocity magnitude $|\tilde{\mathbf{u}}|$ in Ramsey Sound at peak currents during spring and neap tides. Flux across the strait at horizontal transects six Horse Rock half height diameters ($6D$) north and south of Horse Rock are indicated in Table 3. In both, the suggested tidal asymmetry in the ADCP seabed data (Fig. 7b) is apparent, with velocity upstream from Horse Rock being much higher on the spring flood than the spring ebb tide. This is in part driven by "The Bitches", its breadth and shallow depths effectively creating a narrowing of the strait which accelerates the flow in all scenarios covered.

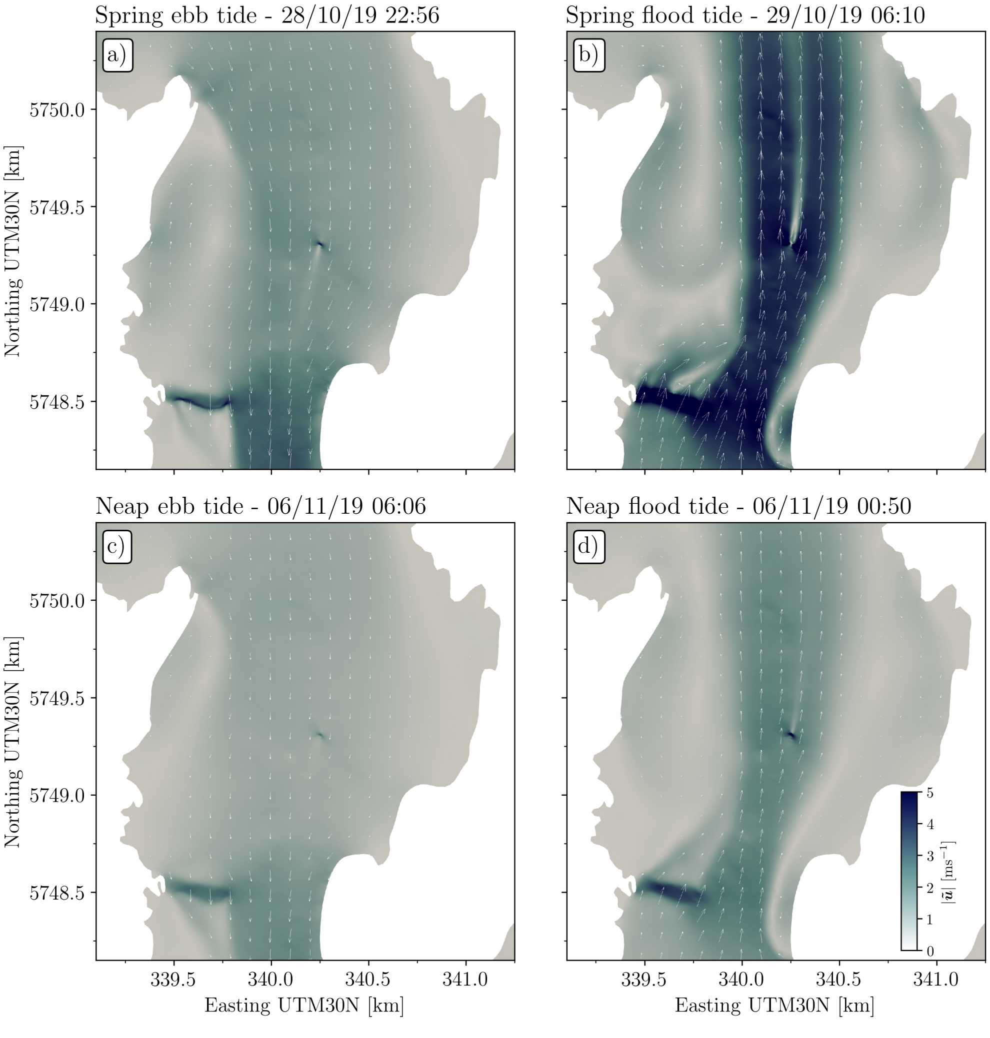

Figure 11: Modelled depth-averaged velocity magnitude $|\tilde{\mathbf{u}}|$ in Ramsey Sound during peak ebb and flood tide velocities under spring and neap conditions.

The amplification of depth-averaged velocity magnitude $|\tilde{\mathbf{u}}|$ on the flood spring tide results in a significant wake structure in lee of Horse Rock. The $|\tilde{\mathbf{u}}|$ upstream from Horse Rock exceeds 5ms^{-1}, a velocity which is maintained on the outer parts of the resulting wake but falls to less than 1ms^{-1} immediately north of the feature, in the inner section of the wake. The width of the wake encompasses roughly a third of the breadth of the strait, featuring recirculation zones on the outer edges. During the spring ebb tide, where Horse Rock

Table 3: Volumetric flow rate (or flux) in m^3s^{-1} in hydrodynamic model at transects spanning the entire channel, six half height diameters of Horse Rock ($6D$) north and south of Horse Rock over spring-neap tidal conditions. Positive values indicate northerly flow

Tide stage	Flux $6D$ South [m^3s^{-1}]	Flux $6D$ North [m^3s^{-1}]
Spring ebb	-49,758	-44,307
Spring flood	76,466	69,601
Neap ebb	-21,087	-18,334
Neap flood	17,769	15,926

pierces the water, a slight reduction in $|\tilde{\mathbf{u}}|$ from roughly 2 to $1ms^{-1}$ occurs, but quickly recovers. Contrary to spring tides, flux across the measured transects is in fact lower on neap flood tide than the equivalent ebb tide. The $|\tilde{\mathbf{u}}|$ in the high velocity sections is clearly greater as the tide floods, but the recirculation zones likely contributes to an overall lower flux value than when the tide is ebbing.

An increase in velocity occurs immediately on top of Horse Rock and "The Bitches" at all instances. In conserving momentum, the drop in depth above these features leads to flow acceleration, and a drop in elevation η for the preservation of energy. The change in depth can also be observed in Fig. 10, where elevation in T4 and T5 is lower than at T6 as they are closer to Horse Rock. Furthermore, velocity glyphs in Fig. 11 illustrate the high degree to which northerly (streamwise) depth-averaged velocity $\tilde{v}$ dominates the magnitude vector of $|\tilde{\mathbf{u}}|$.

In characterising hydrodynamics in Ramsey Sound, the computational mesh is refined to a greater extent around bathymetric features highlighted in Fig. 2, including Horse Rock and "The Bitches". A smaller mesh element size in the areas surrounding these features (minimum $\wedge h$=8m, Fig. 4) permits finer resolution of certain features in Ramsey Sound, as per the bathymetry data and the additional conical structure discussed in Section 3.1.3. Fig. 12 explores how some representative mesh resolutions often utilised in tidal power resource assessment models, which typically do not focus on capturing relatively small bathymetric features, could potentially misrepresent hydrodynamics in the area. The conical feature is removed initially, and the minimum mesh element size $\wedge h$ is subsequently increased from 8m, to 16m, 32m and 64m (Fig. 1). The snapshots indicate peak flood and ebb spring tide, at the same instances as Fig. 11a–b, with internal axes representing easterly $\tilde{u}$, northerly $\tilde{v}$ and magnitude of $|\tilde{\mathbf{u}}|$ depth-averaged velocities at increasing distances from Horse Rock in multiples of its half-height diameter D.

Alterations to the flow structure can be observed with each change in bathymetry characterisation. On the flood tide, the removal of the conical structure induces a reduction in the velocity deficit until roughly $6D$ north, with a disappearance of the wake occurring upon increasing the minimum mesh element size to $\wedge h$=16m. Applying $\wedge h$=32m leads to a redirection of the flow to the south of Horse Rock, in what appears to be the formation of a recirculation zone. This effect can be observed to a greater extent at $\wedge h$=64m. Changes to flow structure on the ebb tide between configurations are subtler than on the flood tide. Beyond the velocity deficit decreasing and subsequently disappearing when removing the conical feature and then increasing to $\wedge h$=16m, respectively, minimal differences can be observed when coarsening the mesh further.

4.3. Regional Dynamics

In generating a hydrodynamic model focused on Ramsey Sound, elevation η and depth-averaged velocities ($\tilde{u}$, $\tilde{v}$ and $|\tilde{\mathbf{u}}|$) are computed within a domain extending far beyond the tidal strait itself. Consequently, flow structures in regions located in the same coastal hydrodynamic system can be analysed. Fig. 13 shows snapshots of depth-averaged velocity $|\tilde{\mathbf{u}}|$ at the same instance as Fig. 11, but at a larger scale. One can observe the full extent of the Horse Rock wake during flood tide, contained within a high velocity jet which reaches

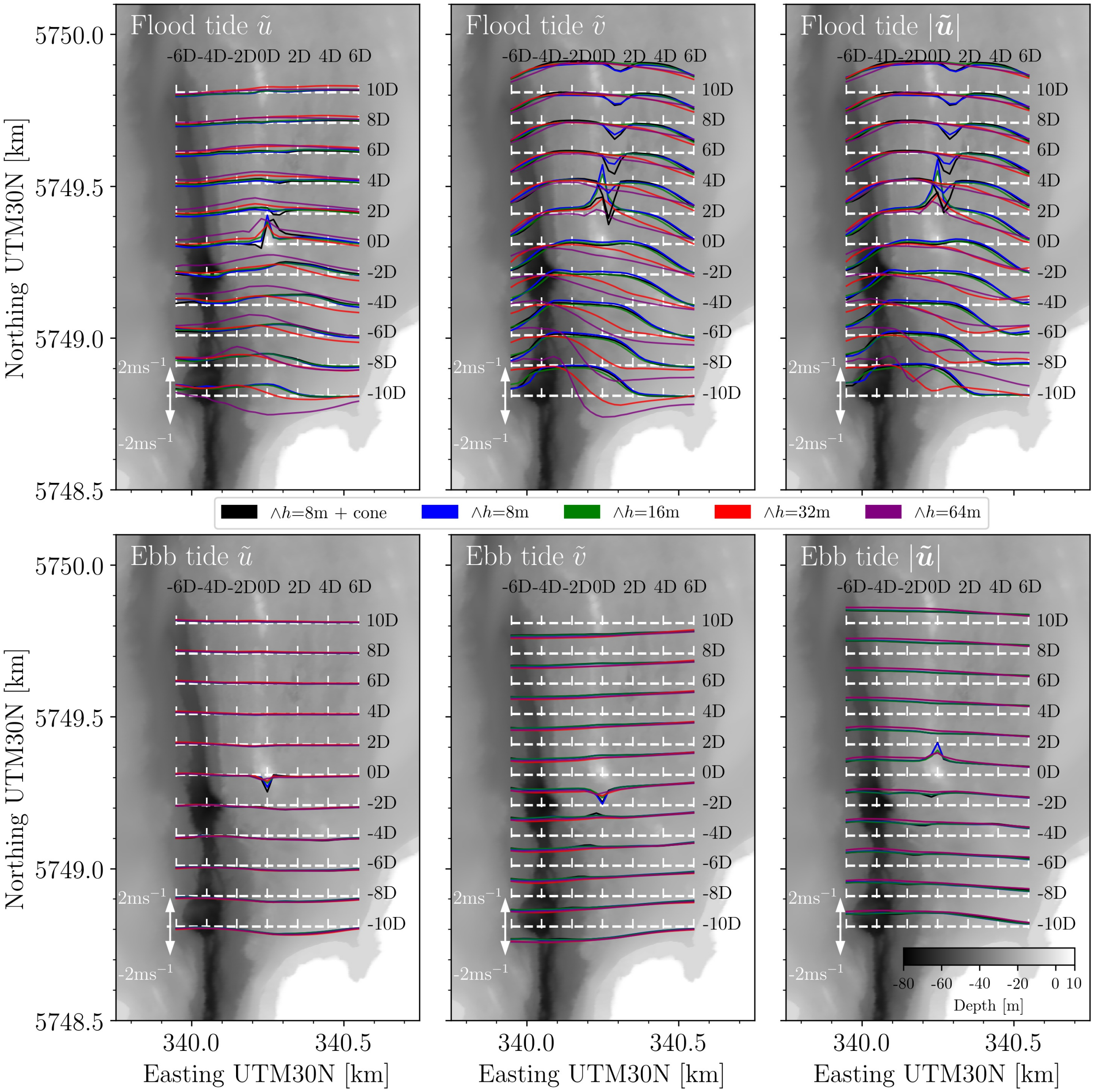

Figure 12: Comparison of spring tide velocity fields in the wake of Horse Rock with 8 (with and without the addition of the cone to the bathymetry), 16, 32 and 64m minimum mesh element sizes $\wedge h$ around bathymetric features. Grid labelling indicates the distance from the tip of horse rock by the half height diameter of Horse Rock D (m). Internal axes indicates velocity.

far beyond the north of Ramsey Island and the conclusion of the wake, curving around the Pembrokeshire coast. A similar, but subtler, effect occurs also on the ebb tide. Notably, these regions of increased velocity appear to be triggered by the narrowing of the strait at "The Bitches". To the west of Ramsey Sound, an array of islands named Bishop and Clerks induce increased current velocities as the tide passes between and around them.

The regional scale vorticity ω is diagnosed by solving a weak form of the vorticity equation (with the corresponding strong or PDE form being $\omega = -\frac{\partial \tilde{u}}{\partial y} + \frac{\partial \tilde{v}}{\partial x}$), as outlined by Vouriot et al. [54]. In Fig. 14, regions of high vorticity appear to stem from "The Bitches", Bishop and Clerks and in some cases, Horse

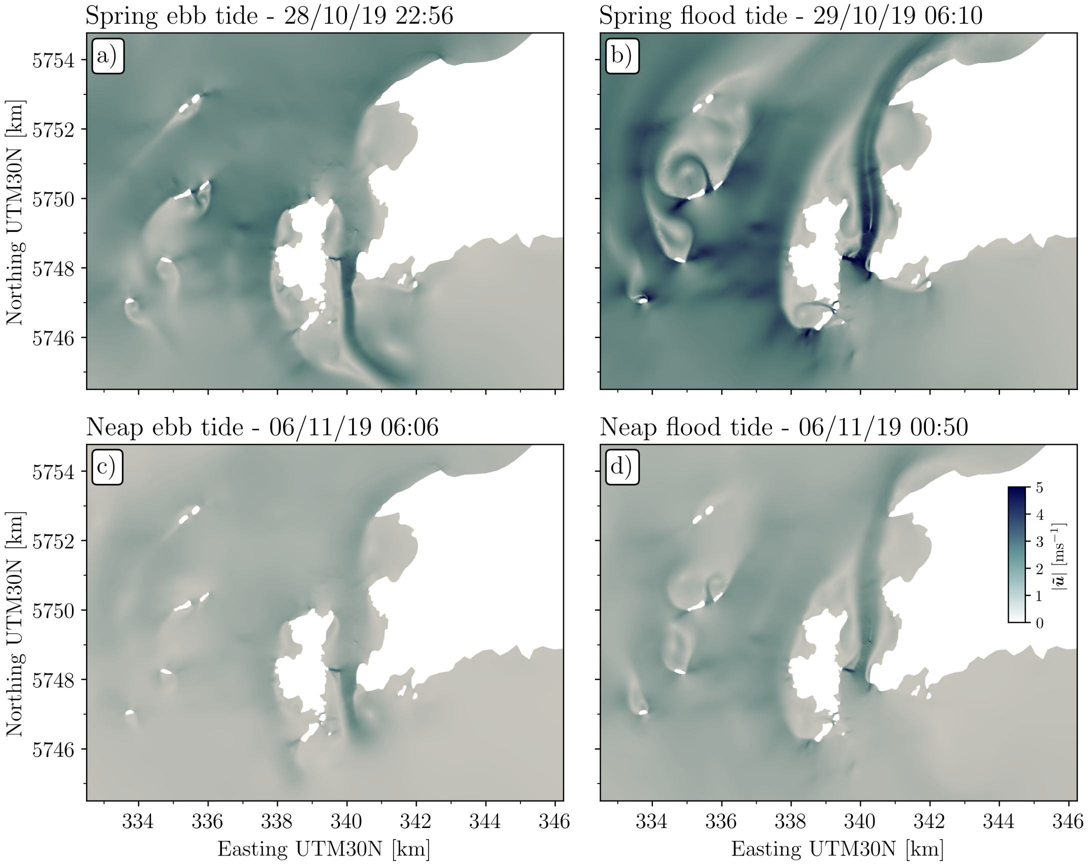

Figure 13: Modelled depth-averaged velocity magnitude $|\tilde{\mathbf{u}}|$ in the coastal regions surrounding Ramsey Sound during peak ebb and flood tide velocities under spring and neap conditions.

Rock. It can be observed how coastal features lead to the formation of pronounced separation zones, that evolve with the the tide.

5. Discussion

5.1. Hydrodynamic characteristics

The following discussion assesses the development of hydrodynamic structures within Ramsey Sound, with particular focus on the manner in which flow interacts with prominent bathymetric features. In this case, the effect of Horse Rock, “The Bitches” and the north-south trench are now discussed. In a further illustration of comments made by Evans et al. [14], Figs. 11 and 13 demonstrate the manner in which these features constructively/destructively interfere with the flow path, generating areas of high velocity considered for the deployment of tidal stream turbines (TSTs). On the southerly ebbing tidal current, flow is accelerated around the headland and into Ramsey Island. It generates a slight wake downstream of Horse Rock, with “The Bitches” then narrowing the channel and driving a jet that dissipates far beyond exiting the strait during spring tide, to a lesser extent at neap tide. Regional flood tide (northwards) velocities are higher than equivalent stages in the spring-neap cycle on the ebb tide, this asymmetry being dictated by the relationship between M_2 and M_4 tidal constituents [33]. However, approach velocities to the tidal strait are actually lower on the flood tide, with the higher regional velocities offset by flow momentum predominantly heading west

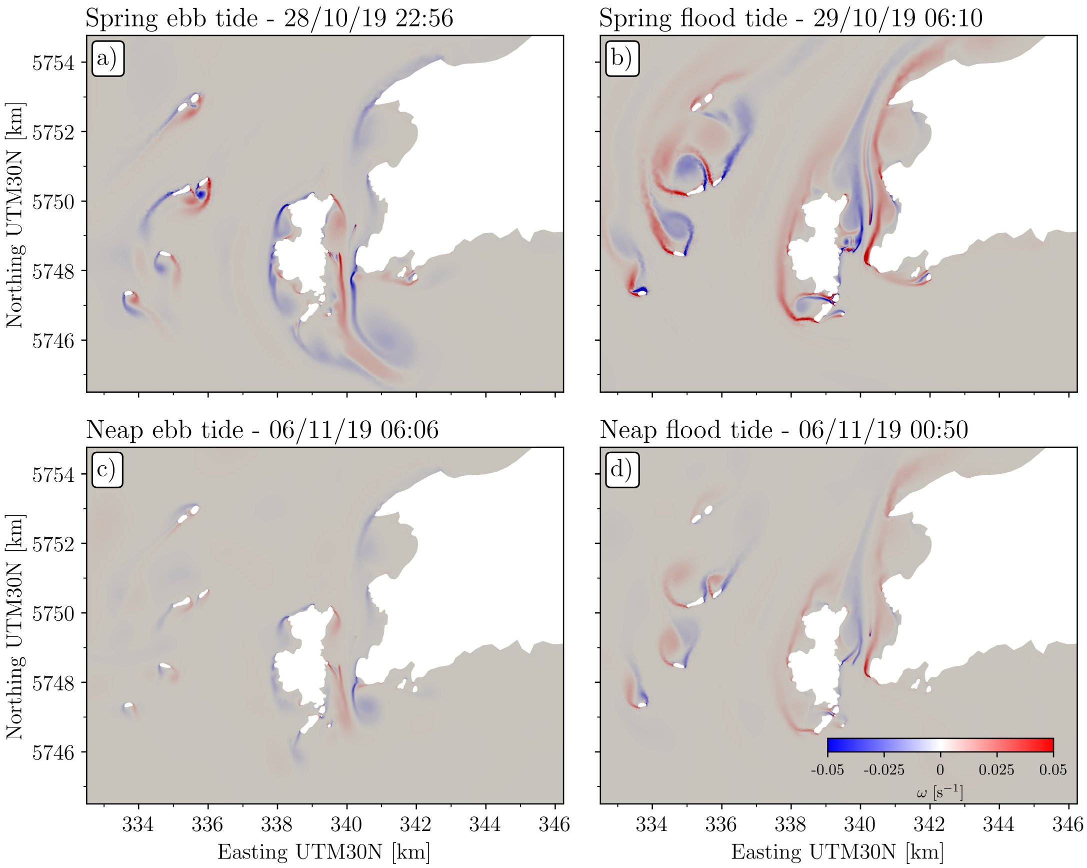

Figure 14: Modelled vorticity around Ramsey Sound and the surrounding waters under different tidal conditions.

of Ramsey Island. The high velocities in the northern section of Ramsey Sound are driven by "The Bitches", the transition from deeper waters, the shape of the coastline which contributes to recirculation zones [53] and flow slowing above, thus diverting around, the north-south trench. This results in flows in excess of 5ms^{-1} passing over Horse Rock during spring tides, which induces a prominent wake structure. A large velocity deficit can be observed immediately downstream, the trace of which only disappears upon exiting the tidal strait. The fact that a wake is significantly less identifiable in other displayed instances suggests that the scale of the velocity deficit in submerged features is predominantly dictated by the magnitude of the streamwise velocity. This is highlighted by the fact that during the ebb spring tide, even though Horse Rock is piercing the water, a much smaller wake is produced than on the flood tide equivalent, triggered by the lower streamwise velocities (Table 3).

Certain considerations must be made with regards to these observed flow structures and the resulting implications on how TSTs would be deployed and operated. The available power P from a stream of water is approximately proportional to the cube of the unperturbed fluid speed ν (as shown by $P \propto \nu^3$) [55], highlighting the advantage of TST deployment in higher velocity areas. The velocity deficit experienced downstream of Horse Rock on the high current flood tide could therefore have a significant bearing on the performance of TSTs, requiring strategic positioning to avoid both the wake as well as the lower velocity zones either side of the high velocity central flow. Furthermore, misaligning the axial flow on a TST has been shown to have negative consequences on performance and durability [56], a potential factor highlighted by the high vorticity in the lee of Horse Rock (Fig. 14). Construction of multiple TSTs would also need to consider the interactions of the resulting turbine wakes with existing submerged features. Considering the sensitivity of the flow path to these bathymetric features, further complications could arise should TSTs redirect the flow in a manner which erodes or changes bathymetric structures. The effect of altering the geometry of Horse Rock is demonstrated in Fig. 12, where a coarsening of the mesh serves to trim the tip of Horse Rock, affecting the computed flow with each increase of minimum mesh element size $\wedge h$. Additionally, altering the composition of the rocky reef "The Bitches" could dramatically affect the favourable flow acceleration it contributes to. Adaptation to potential changes, such as the ability of a TST to yaw, could thus prove advantageous [57]. This discussion highlights several important points: the performance of an array of TSTs is highly dependent on underlying flow structure, but in turn this flow structure is itself highly dependent on geometrical structure, and computational estimates of this is further dependent on mesh resolution and geometry representation; these points are expanded upon in the following sections.

5.2. Model considerations

The complexity of the flow structure in Ramsey Sound and the implications on how TSTs would be deployed and operated to harness it has been outlined in the previous section. Therefore, sufficient representation of the hydrodynamics is required to model and maximise the performance and reliability of potential projects. The impact of the considered model aspects in characterising the flow regime is discussed herein.

5.2.1. Seabed roughness coefficient

The availability of both vessel- and seabed-mounted ADCP survey data within Ramsey Sound provides a high spatial and temporal range over which to calibrate the depth-averaged model. Furthermore, the calibration process serves as a diagnostic in assessing the impact of physical parameter representation. This study explores how variable characterisation of bed shear stress τ_b via Manning's coefficient n, a parameter which many tidal energy resource assessment modelling studies treat as a constant in space, can influence the agreement of the numerical model with the measured data. British Geological Survey (BGS) bed class data permits the application of a variable Manning coefficient field N (Table 1, Fig. 4a–b), which can be scaled throughout the domain (e.g. $1.25N$) or locally in Ramsey Sound (e.g. $1.25N^*$ as per Fig. 4c). Figs. 6–9 and Table 2 provide a comparison between samples of measured datasets and equivalent data extracted from the numerical model applying different Manning coefficient fields. Tidal elevation η (Fig. 7a) and constituent amplitude α and phase ϕ (Fig. 6) data are barely altered between different configurations of the model, except in areas which are subject to a particularly high n value. The highest constituent data discrepancies are in the Severn Estuary, which has large areas exhibiting over $0.05\text{sm}^{-1/3}$, classified as bedrock. A higher sensitivity to changes in n is observed in local velocities, with improved model agreement occurring in the scaled configurations of the variable field N. This justifies the use of variable scaling N^* as a tool for localised tuning of the physical representation in the area of interest, where the required optimisation of velocities might not reflect the scaling required to maximise the agreement in elevations elsewhere. Validation against ADCP survey data provides an illustration of the temporal and spatial effect of altering the Manning coefficient field on velocity magnitude $|\tilde{\mathbf{u}}|$ in Ramsey Sound. It is clear in Fig. 8 that characterisation of the flow is superior during the high current stages of the tidal cycle, with poor correlation during slack tides. Generation from TSTs will predominantly occur during periods of high flow velocity, so slack tide error in the model is perhaps not a major issue for tidal resource assessment applications.

By integrating seabed composition data into the numerical model, specifically the representation of bed shear stress throughout the domain, this study has demonstrated the potential importance of considering this as a variable rather than a uniform field. However, it is notable that little variation exists in the BGS dataset in characterising the seabed in Ramsey Sound itself. Furthermore, coastal and intertidal sections of the domain apply an estimation of bed class due to a lack of data. Admiralty Charts suggest a more diverse seabed composition than is afforded by the BGS data, describing zones with indistinct borders consisting of 'rock', 'sand, gravel, mud' and 'sand, shells' [31] in areas all denoted by 'medium gravel' in the BGS data. A more detailed survey than carried out by BGS, specific to Ramsey Sound, could prove beneficial. If required, a more nuanced approach than the scaling method implemented herein could apply discrete changes between bed class as a guide to tuning seabed friction. Alternatively, an adjoint approach has been shown to accurately infer Manning coefficient data spatially from harmonic tidal constituents [58].

5.2.2. Mesh resolution

In applying a computational mesh with minimum element size $\wedge h$=8m around key bathymetric features (Fig. 1d), the mesh is refined to a much greater extent than is currently typical of tidal stream resource assessment studies. A diagram of the effects of increasing $\wedge h$ on the geometry of Horse Rock is provided in Fig. 3, including the inclusion of a conical structure which is applied in the main configuration of the model. Fig. 12 demonstrates the necessity of applying such a refined mesh in capturing the complex flow structures in Ramsey Sound. Even coarsening resolution to $\wedge h$=16m, what would still be considered quite a fine mesh, much of the wake structure on the flood tide is no longer captured. A further coarsening to $\wedge h$=32m actually leads to a redirection of the upstream flow. This is likely a result of the manner in which the geometry of "The Bitches" is altered when it is discretised, as it has a governing influence on the flow regime in Ramsey Sound. Similar to the scale of the wake structure discussed in Section 5.1, the smaller overall hydrodynamic changes in the ebb tide when increasing $\wedge h$ suggests that use of the most highly refined mesh resolutions surrounding prominent bathymetric features is less vital at lower velocities. However, the impact of implementing the conical structure also evident on the ebb tide, its application causing Horse Rock to pierce the water thus forming a wake. This highlights the need to appropriately capture submergence, or lack thereof, of bathymetric features at all stages of the tidal cycle, as piercing the water could induce significant change in the flow structure. As the 2m bathymetry data misrepresents the water-piercing peak of Horse Rock clearly indicated in other accounts, special consideration in characterising the manner in which obstructive features remain submerged may be required for tidal resource assessments exhibiting similar features. Insufficient characterisation of the flow regime, both through an under-refined mesh or incomplete bathymetry dataset over non-coastal intertidal areas, could have significant implications in the way turbines are deployed or operated. The poor reproduction of easterly (non-streamwise) depth-averaged velocities $\tilde{u}$, as shown in Table 2, suggests that a similar artificial feature could improve the characterisation of "The Bitches" and thus overall model validation. It is also worth noting that model interpretation of regional velocities should take into account coarser mesh resolution further from the immediate areas of interest. The vorticity metric, for example, is very sensitive to mesh refinement and could partly explain why vorticity is highest in Ramsey Sound (Fig. 14), where the mesh element size is the smallest.

5.2.3. Representation of the water column

Depth-averaged models are commonly applied in regional scale tidal energy resource assessment studies due to their computational efficiency and the well-mixed conditions established in these sites, yet some previous studies recommend 3D modelling in characterising hydrodynamics in Ramsey Sound [14, 17]. In Fig. 10, up-welling and water column velocity variations on the flood tide in the lee of the submerged feature Horse Rock indicate the presence of notable 3D flow structure, a factor much less evident on the ebb tide. However, the efficiency of the model permits simulations under a wide range of different physical parameters, prompting sufficient calibration with the available measured datasets. Whilst a 3D model would likely provide a more accurate representation of the hydrodynamics immediately around Horse Rock and "The Bitches", its relative computational cost may limit tuning possibilities as well as TST array micro-siting design optimisation scope [59]. Furthermore, the desired accuracy in calibrating a 3D model may require a more comprehensive dataset than is available here. At peak flow, as shown in Fig. 9, underestimation of velocity magnitude is present with all model configurations. The lack of temporally variant data in these key, highly dynamic areas, renders more accurate flow characterisation a challenging task. More holistic methods for measuring flow velocities in such areas, such as with radar derived velocity fields, may support sourcing of data for validating a 3D model.

6. Conclusions

This study combines measured survey data with depth-averaged modelling in investigating hydrodynamics in Ramsey Sound, Wales. The tidal strait is an area exhibiting high velocity currents considered for the testing and/or deployment of tidal stream turbines (TSTs). Ramsey Sound is notable for its variety of prominent bathymetric features which significantly influence localised and regional flow structures. On spring flood tides, rocky reefs called "The Bitches" narrow the channel causing regions of high velocity and vorticity which in turn induce large velocity deficits and recirculation zones in the wake of a submerged pinnacle, Horse Rock. We can observe a smaller wake during the spring ebb tide, due to lower flux and wider spread of the upstream flow path, and despite the tip of Horse Rock drying at this stage. The sensitivity of the flow structure to the geometry of Horse Rock via coarsening of the computational mesh highlights the importance of accurately representing small but influential features. In areas which experience drying at certain stages of the tide, ensuring a correct model representation is beneficial in characterising tidal hydrodynamics.

Model calibration is supported by a multitude of measured datasets covering a range of locations and timescales. We investigate the impact of common simplifications in tidal energy resource assessment studies. The required low mesh element size to characterise bathymetric features, and the hydrodynamic structures they influence, highlights the need for such studies to consider a more refined mesh than is commonly applied to these areas. Furthermore, localised scaling of a variable Manning coefficient field is identified as a useful tuning parameter in optimising the representation of tidal velocities and elevations throughout the domain. We recommend a more nuanced approach than numerical scaling, perhaps combining discrete alterations in bed class with a seabed sediment survey more focused in key areas than available here. Despite the immediate wake regions of Horse Rock displaying 3D flow characteristics during the flood tide, 2D modelling can be appropriate for the optimisation of TST configuration, especially considering the high correlation between modelled and measured data during energetic peak flows. Meanwhile, 3D modelling studies may benefit from survey data exhibiting higher temporal variability. There might be opportunities in nesting high-fidelity 3D models within regional depth-averaged models, accounting for the far-field 2D effects that influence the immediate area of interest.

Acknowledgements

LM would like to acknowledge the financial support of an EPSRC PhD studentship award. AA acknowledges the support of NERC through the Industrial Innovation fellowship grant NE/R013209/2. MP acknowledges support from EPSRC under grants EP/M011054/1, EP/L000407/1, EP/R029423/1. The authors also thank Dr Chris Wooldridge for skippering the R/V *Guiding Light* during data collection, and Tidal Energy Limited (TEL) for providing the seabed measurements and their valuable input. Intertek Energy and Water Consultancy Services support this innovative research, and further information can be found at: http://www.intertek.com/energy-water/tidal-energy/

CRediT authorship contribution statement

Lucas Mackie: Conceptualization, Methodology, Software, Validation, Formal Analysis, Investigation, Writing - original draft, Visualization. **Paul S. Evans:** Resources, Writing - review & editing. **Magnus J. Harrold:** Resources , Writing - review & editing. **Tim O'Doherty:** Writing - review & editing. **Matthew D. Piggott:** Conceptualization, Writing - review & editing, Supervision, Funding Aquisition. **Athanasios Angeloudis:** Conceptualization, Methodology, Investigation, Writing - review & editing, Supervision, Funding Aquisition.

References

[1] S. P. Neill, A. Angeloudis, P. E. Robins, I. Walkington, S. L. Ward, I. Masters, M. J. Lewis, M. Piano, A. Avdis, M. D. Piggott, G. Aggidis, P. Evans, T. A. Adcock, A. Zidonis, R. Ahmadian, R. Falconer, Tidal range energy resource and optimization – past perspectives and future challenges, Renewable Energy 127 (2018) 763–778.

[2] M. Lewis, S. P. Neill, P. E. Robins, M. R. Hashemi, Resource assessment for future generations of tidal-stream energy arrays, Energy (2015).

[3] I. Fairley, S. Neill, T. Wrobelowski, M. Willis, I. Masters, Potential array sites for tidal stream electricity generation in Pembrokeshire, in: 9th European Wave and Tidal Energy Conference, 2011, pp. 1–8. URL: `https://www.researchgate.net/publication/260435853_Potential_array_sites_for_tidal_stream_electricity_generation_in_Pembrokeshire`.

[4] D. Chen, G. H. Jirka, Experimental study of plane turbulent wakes in a shallow water layer, Fluid Dynamics Research (1995).

[5] P. M. Lloyd, P. K. Stansby, D. Chen, Wake formation around islands in oscillatory laminar shallow-water flows. Part 1. Experimental investigation, Journal of Fluid Mechanics (2001).

[6] C. J. Baker, The turbulent horseshoe vortex, Journal of Wind Engineering and Industrial Aerodynamics (1980).

[7] E. Wolanski, W. M. Hamner, Topographically controlled fronts in the ocean and their biological influence, Science (1988).

[8] E. Wolanski, J. Imberger, M. L. Heron, Island wakes in shallow coastal waters, Journal of Geophysical Research (1984).

[9] B. Guo, R. Ahmadian, P. Evans, R. A. Falconer, Studying the Wake of an Island in a Macro-Tidal Estuary, Water 12 (2020).

[10] L. White, E. Deleersnijder, Diagnoses of vertical transport in a three-dimensional finite element model of the tidal circulation around an island, Estuarine, Coastal and Shelf Science (2007).

[11] A. Pérez-Ortiz, A. G. Borthwick, J. McNaughton, A. Avdis, Characterization of the tidal resource in rathlin sound, Renewable Energy 114 (2017) 229 – 243. Wave and Tidal Resource Characterization.

[12] R. Martinuzzi, C. Tropea, The flow around surface-mounted, prismatic obstacles placed in a fully developed channel flow: (Data bank contribution), Journal of Fluids Engineering, Transactions of the ASME (1993).

[13] P. Ouro, C. A. M. E. Wilson, P. Evans, A. Angeloudis, Large-eddy simulation of shallow turbulent wakes behind a conical island, Physics of Fluids 29 (2017) 126601.

[14] P. Evans, A. Mason-Jones, C. Wilson, C. Wooldridge, T. O'Doherty, D. O'Doherty, Constraints on extractable power from energetic tidal straits, Renewable Energy 81 (2015) 707–722.

[15] A. S. Bahaj, L. E. Myers, Shaping array design of marine current energy converters through scaled experimental analysis, Energy (2013).

[16] Miller, Jack and Hornigold, Thomas, Marine Renewables: UK Parliament POSTnote, 2020. URL: `https://post.parliament.uk/research-briefings/post-pn-0625/`.

[17] D. Haverson, J. Bacon, H. C. Smith, V. Venugopal, Q. Xiao, Modelling the hydrodynamic and morphological impacts of a tidal stream development in Ramsey Sound, Renewable Energy 126 (2018) 876 – 887.

[18] E. Zangiabadi, I. Masters, A. Williams, C. T.N., Characterisation of the Coastal Hydrology of Oceans Using 3D Computational Fluid Dynamics, in: 4th International Conference on Ocean Energy, Dublin, Ireland, 2012, pp. 1–6.

[19] I. Milne, A. Day, R. Sharma, R. Flay, The characterisation of the hydrodynamic loads on tidal turbines due to turbulence, Renewable and Sustainable Energy Review 56 (2016) 851–864.

[20] The Crown Estate, UK Wave and Tidal Key Resource Areas Project: Summary Report), 2012. URL: `http://www.marineenergywales.co.uk/wp-content/uploads/2016/01/Summary-Report-FINAL.pdf`.

[21] S. Draper, T. Adcock, A. Borthwick, G. Houlsby, Estimate of the tidal stream power resource of the Pentland Firth, Renewable Energy 63 (2014) 650–657.

[22] T. Kärnä, S. C. Kramer, L. Mitchell, D. A. Ham, M. D. Piggott, A. M. Baptista, Thetis coastal ocean model: Discontinuous Galerkin discretization for the three-dimensional hydrostatic equations, Geoscientific Model Development 11 (2018) 4359–4382.

[23] D. Coles, L. Blunden, A. Bahaj, Assessment of the energy extraction potential at tidal sites around the Channel Islands, Energy 124 (2017) 171–186.

[24] T. Adcock, S. Draper, G. Houlsby, A. Borthwick, On the tidal resource of the Pentland Firth, in: 4th International Conference on Ocean Energy, Dublin, Ireland, 2012, pp. 1–5.

[25] S. Serhadlioğlu, T. A. Adcock, G. T. Houlsby, S. Draper, A. G. Borthwick, Tidal stream energy resource assessment of the Anglesey Skerries, International Journal of Marine Energy (2013).

[26] M.-S. R., J. Hill, S. C. Kramer, A. Avdis, P. A. Allison, M. D. Piggott, Tidal resource extraction in the Pentland Firth, UK: Potential impacts on flow regime and sediment transport in the Inner Sound of Stroma, Renewable Energy 76 (2015) 596–607.

[27] S. W. Funke, S. C. Kramer, M. D. Piggott, Design optimisation and resource assessment for tidal-stream renewable energy farms using a new continuous turbine approach, Renewable Energy 99 (2016) 1046–1061.

[28] N. Guillou, G. Chapalain, Numerical simulation of tide-induced transport of heterogeneous sediments in the english channel, Continental Shelf Research 30 (2010) 806–819.

[29] J. Thiébot, P. B. du Bois], S. Guillou, Numerical modeling of the effect of tidal stream turbines on the hydrodynamics and the sediment transport – application to the alderney race (raz blanchard), france, Renewable Energy 75 (2015) 356 – 365.

[30] British Oceanographic Data Centre, UK Tide Gauge Network Data, Technical Report, British Oceanographic Data Centre, 2017. URL: `https://www.bodc.ac.uk/data/hosted_data_systems/sea_level/uk_tide_gauge_network/processed/`.

[31] GPS Nautical Charts, A Ramsey Sound with The Bishops and Clerks (Marine Chart : 1482 1), 2014. URL: `http://www.gpsnauticalcharts.com/main/1482_1-a-ramsey-sound-with-the-bishops-and-clerks-nautical-chart.html`.

[32] S. L. Ward, P. E. Robins, M. J. Lewis, G. Iglesias, M. R. Hashemi, S. P. Neill, Tidal stream resource characterisation in progressive versus standing wave systems, Applied Energy 220 (2018) 274–285.

[33] P. E. Robins, S. P. Neill, M. J. Lewis, S. L. Ward, Characterising the spatial and temporal variability of the tidal-stream energy resource over the northwest European shelf seas, Applied Energy (2015).

[34] M. Togneri, I. Masters, Comparison of marine turbulence characteristics for some potential turbine installation sites, Proceedings of the 4th International Conference on Ocean Energy (2012).

[35] W. Pan, S. C. Kramer, M. D. Piggott, Multi-layer non-hydrostatic free surface modelling using the discontinuous galerkin method, Ocean Modelling 134 (2019) 68–83.

[36] F. Rathgeber, D. A. Ham, L. Mitchell, M. Lange, F. Luporini, A. T. T. McRae, G.-T. Bercea, G. R. Markall, P. H. J. Kelly, Firedrake: automating the finite element method by composing abstractions, ACM Transactions on Mathematical Software 43 (2016) 24:1 – 24:27.

[37] T. Kärnä, B. de Brye, O. Gourgue, J. Lambrechts, R. Comblen, V. Legat, E. Deleersnijder, A fully implicit wetting–drying method for DG-FEM shallow water models, with an application to the Scheldt Estuary, Computer Methods in Applied Mechanics and Engineering 200 (2011) 509–524.

[38] A. Angeloudis, S. C. Kramer, A. Avdis, M. D. Piggott, Optimising tidal range power plant operation, Applied Energy 212 (2018) 680–690.

[39] F. Harcourt, A. Angeloudis, M. D. Piggott, Utilising the flexible generation potential of tidal range power plants to optimise economic value, Applied Energy 237 (2019) 873–884.

[40] A. Angeloudis, S. C. Kramer, N. Hawkins, M. D. Piggott, On the potential of linked-basin tidal power plants: An operational and coastal modelling assessment, Renewable Energy 155 (2020) 876–888.

[41] A. L. Baker, R. M. Craighead, E. J. Jarvis, H. C. Stenton, A. Angeloudis, L. Mackie, A. Avdis, M. D. Piggott, J. Hill, Modelling the impact of tidal range energy on species communities, Ocean & Coastal Management 193 (2020) 105221.

[42] S. Balay, S. Abhyankar, M. F. Adams, J. Brown, P. Brune, K. Buschelman, L. Dalcin, V. Eijkhout, W. D. Gropp, D. Kaushik, M. G. Knepley, L. C. McInnes, K. Rupp, B. F. Smith, S. Zampini, H. Zhang, H. Zhang, PETSc Users Manual, Technical Report ANL-95/11 - Revision 3.7, Argonne National Laboratory, 2016. URL: `http://www.mcs.anl.gov/petsc`.

[43] A. Avdis, A. S. Candy, J. Hill, S. C. Kramer, M. D. Piggott, Efficient unstructured mesh generation for marine renewable energy applications, Renewable Energy 116 (2018) 842–856.

[44] C. Geuzaine, J.-F. Remacle, Gmsh Reference Manual, Technical Report 4.6.0, GNU General Public License, 2020. URL: `https://gmsh.info/`.

[45] Seazone Solutions Ltd., Edina Digimap Service, Hydrospatial one, gridded bathymetry, 2014. URL: `http://digimap.edina.ac.uk/marine/`.

[46] Bangor University, UK Tide Gauge Network Data, Technical Report, Bangor University, 2017?

[47] G. D. Egbert, S. Y. Erofeeva, Efficient Inverse Modeling of Barotropic Ocean Tides, Atmos. Oceanic Technol. (2002) 183–204.

[48] YouTube, Horse Rock, Ramsey Sound, Pembrokeshire, 2014. URL: `https://www.youtube.com/watch?v=o1PQSwHkxjk`, Upload User: utubemematt, Accessed: 11/06/2020.

[49] British Geological Survey, BGS Geology: marine sediments 250k — DigSBS250, 2011. URL: `https://www.bgs.ac.uk/products/offshore/DigSBS250.html`.

[50] R. L. Soulsby, Tidal current boundary layers, in: B. Le Mehaute, D. M. Hanes (Eds.), The Sea, Volume 9: Ocean Engineering Science, volume 9, Harvard University Press, 2005, pp. 0–10.

[51] Tidal Energy Limited, DeltaStream Demonstration Ramsey Sound, Pembrokeshire: Scoping Report, 2008. URL: `https://tethys.pnnl.gov/sites/default/files/publications/TEL_Scoping_Report_2008.pdf`.

[52] P. Evans, E. Lazarus, A. Mason-Jones, D. O'Doherty, T. O'Doherty, Wake Characteristics of a Natural Submerged Pinnacle and Implications for Tidal Stream Turbine Installations, in: 11th European Wave and Tidal Energy Conference, 2015, pp. 1–10. URL: `https://www.researchgate.net/publication/281589471_Wake_characteristics_of_a_natural_submerged_pinnacle_and_implications_on_tidal_stream_turbine_installations`.

[53] P. Evans, S. Armstrong, C. Wilson, I. Fairley, C. Wooldridge, I. Masters, Characterisation of a Highly Energetic Tidal Energy Site with Specific Reference to Hydrodynamics and Bathymetry, in: 10th European Wave and Tidal Energy Conference, 2013, pp. 1–11. URL: `https://www.researchgate.net/publication/257869016_Characterisation_of_a_Highly_Energetic_Tidal_Energy_Site_with_Specific_Reference_to_Hydrodynamics_and_Bathymetry`.

[54] C. V. M. Vouriot, A. Angeloudis, S. C. Kramer, M. D. Piggott, Fate of large-scale vortices in idealized tidal lagoons, Environmental Fluid Mechanics 19 (2019) 329–348.

[55] A. S. Bahaj, Generating electricity from the oceans, Renewable and Sustainable Energy Reviews 15 (2011) 3399–3416.

[56] C. Frost H., P. S. Evans, M. J. Harrold, A. Mason-Jones, T. O'Doherty, D. O'Doherty, The impact of axial flow misalignment on a tidal turbine, Renewable Energy 113 (2017) 1333–1344.

[57] C. Frost, C. Morris, A. Mason-Jones, D. O'Doherty, T. O'Doherty, The effect of tidal flow directionality on tidal turbine performance characteristics, Renewable Energy 78 (2015) 609–620.

[58] S. Warder, A. Angeloudis, S. C. Kramer, C. Cotter, M. Piggott, A comparison of bayesian inference and gradient-based approaches for friction parameter estimation, EarthArXiv (2020).

[59] S. Funke, P. Farrell, M. Piggott, Tidal turbine array optimisation using the adjoint approach, Renewable Energy 63 (2014) 658 – 673.